*J. Fluid Mech.* (1994), *vol.* 280, *pp.* 255–285



# Melting driven by vigorous compositional convection

By ROSS C. KERR

Research School of Earth Sciences, The Australian National University, Canberra, ACT 0200, Australia

(Received 11 March 1993 and in revised form 17 June 1994)

The melting of a solid in contact with a hot fluid is quantified for the case in which a difference between the densities of the fluid and of the melted solid is able to drive vigorous compositional convection. A scaling analysis is first used to obtain a theoretical expression for the melting rate that is valid for a certain range of Stefan numbers. This expression is then compared with melting velocities measured in laboratory experiments in which ice and wax are melted when they are overlain or underlain by hot aqueous solutions. The melting velocities are consistent with the theoretical expression, and are found to depend on the heats of solution that are released when the melted solids mix with the solutions. The experiments also indicate that, for vigorous convection to occur during the melting of a floor, the unstable compositional buoyancy needs to be at least twice the stabilizing thermal buoyancy.

An important geological situation in which melting occurs is when large volumes of basaltic magma are intruded into the Earth's continental crust. The theoretical and experimental results are used and extended to examine quantitatively the melting of the floor and walls of the magma chamber, and of crustal blocks that fall into the chamber.

## 1. Introduction

An everyday means of producing a refreshingly cold drink is to add ice cubes to a glass of water. A similar result is achieved if ice cubes are added to a glass of Scotch. However, if both drinks are made simultaneously it will be discovered that the ice melts *faster* in the Scotch, a result that is due to the simple fact that the thermal convection that supplies heat to melt the ice is augmented by the *compositional convection* that arises because the melt water is denser than the underlying alcohol-rich Scotch. Such compositionally driven melting is the focus of this paper.

Melting driven by compositional convection also arises if a hot fluid melts an underlying solid and the density of the resulting melt is less than that of the fluid. This situation has been explored experimentally by Campbell (1986), Huppert & Sparks (1988*a*) and Woods (1991), who all found that the compositional convection dramatically increases the rate of melting over what would otherwise occur due solely to thermal diffusion. This observation is of geological interest because it suggests that large volumes of hot dense basaltic magma intruded into the Earth's continental crust can melt and mix with the crust to produce hybrid melts.

The fundamental aim of the present paper is to quantify the rate at which compositionally driven melting occurs. The paper follows several recent investigations that have similarly examined the rate at which melting occurs when it is driven by thermal convection (Huppert & Sparks 1988*b*, *c*), by forced turbulent flow (Huppert 1989), or by thermal or compositional diffusion (Woods 1992).

I begin in §2 by using a scaling analysis to predict the rate of melting of a horizontal floor or roof. This analysis is compared in §3 with a series of experiments in which either wax or ice is melted by being placed in contact with hot aqueous solutions. Several interesting experimental results are then discussed in §4. Finally in §5 the results are extended and applied to quantify the melting that arises when basaltic magma invades the Earth's crust.

## 2. Scaling theory

Consider the melting of a solid of composition $C_s$, melting temperature $T_m$ and uniform initial temperature $T_s$, overlain by a fluid with a composition $C_f$ and temperature $T_f$ (figure 1). If the volume of fluid is large, the far-field conditions will not change, and it is expected that the solid will melt at a constant velocity $V$. I shall assume that the interface between the solid and the melt is flat, and that thermal effects on the densities of the fluid and melt are negligible in comparison to compositional effects. I also note that this paper is focused exclusively on melting rather than dissolving; in this regime, which will apply if $T_f$ is significantly greater than $T_m$ (Woods 1992), compositional diffusion can be neglected in comparison to thermal diffusion, so that there is a sharp step in the compositional profile.

The aim is to use scaling theory to determine $V$ in the case where melting of the solid leads to vigorous compositional convection, a situation that can only occur if the density $\rho_m$ of the melt is less than the density $\rho_f$ of a hot overlying fluid (or alternatively if the melt is denser than a hot underlying fluid). As is illustrated in figure 1, a thin boundary layer of buoyant melt is envisaged that continually grows and periodically detaches to drive this convection. The timescale $\tau$ and wavelength $\lambda$ for exponential growth of the fastest-growing linear Rayleigh–Taylor instabilities to this buoyant layer (Odé 1966; Lister & Kerr 1989) are given by

$$\tau = P\left(\frac{\mu_f}{\mu_m}\right)\frac{\mu_m}{gh_m(\rho_f-\rho_m)} \quad \text{and} \quad \lambda = Q\left(\frac{\mu_f}{\mu_m}\right)\pi h_m, \tag{1}$$

where $g$ is the acceleration due to gravity, $h_m$ is the thickness of this layer, $\mu_m$ and $\mu_f$ are the viscosities of the melt and hot fluid, and the functions $P(\mu_f/\mu_m)$ and $Q(\mu_f/\mu_m)$, shown in figure 2, have the respective values of 10.2988... and 1.1822... for $\mu_f = \mu_m$, and have the asymptotic limits of

$$P(\mu_f/\mu_m) = 6.222\ldots \quad \text{and} \quad Q(\mu_f/\mu_m) = 0.94\ldots \quad \text{for} \quad \mu_f \ll \mu_m, \tag{2a}$$

and

$$P\left(\frac{\mu_f}{\mu_m}\right) = (324)^{1/3}\left(\frac{\mu_f}{\mu_m}\right)^{2/3} \quad \text{and} \quad Q\left(\frac{\mu_f}{\mu_m}\right) = \left(\frac{2}{3}\right)^{1/3}\left(\frac{\mu_f}{\mu_m}\right)^{1/3} \quad \text{for} \quad \mu_f \gg \mu_m. \tag{2b}$$

The typical thickness of the melt layer can be predicted from the argument, also used both in Lister & Kerr (1989, §5) and in Kerr & Lister (1992, Appendix), that the time to grow the melt layer, $h_m/V$, must be comparable to the timescale, $\tau$, of the gravitational instabilities that drain the layer and drive the overlying compositional convection. This argument leads to the estimates

$$\tau \sim \left(\frac{P\mu_m}{gV(\rho_f-\rho_m)}\right)^{1/2} \tag{3}$$

and

$$h_m \sim \left(\frac{PV\mu_m}{g(\rho_f-\rho_m)}\right)^{1/2}. \tag{4}$$

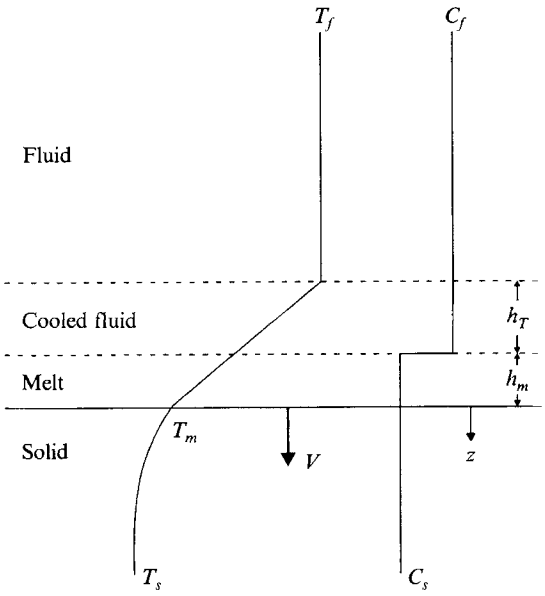


FIGURE 1. Schematic diagram of the envisaged intermediate layers of melted solid and cooled fluid (see §2) during the melting at velocity $V$, driven by vigorous compositional convection, of a solid that is in contact with a hot fluid. The figure also indicates the envisaged thermal and compositional profiles. At the interface, kinetic effects (e.g. Kuo & Kirkpatrick 1985; Oxtoby 1990) are neglected and the temperature is assumed to be the equilibrium melting temperature $T_m$. Although the temperature profile through the intermediate layers is sketched as linear, its actual shape will depend on $k_f/k_m$ and $\mathscr{S}$.

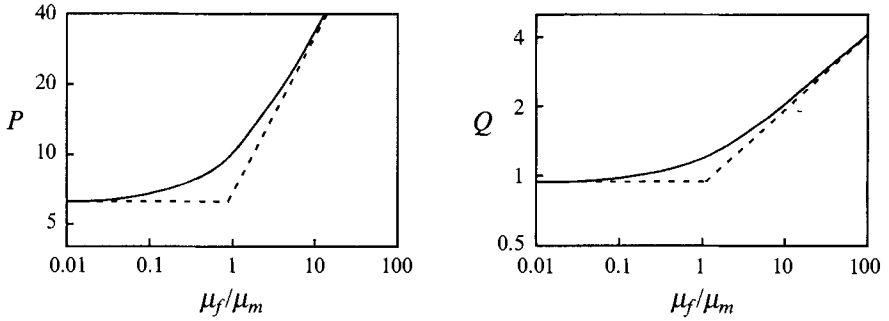


FIGURE 2. The functions $P(\mu_f/\mu_m)$ and $Q(\mu_f/\mu_m)$ defined by (1).

Turning now to the temperature field, it is first noted that the temperature in the solid is given by

$$T(z) = T_s + (T_m - T_s)\,\mathrm{e}^{-Vz/\kappa_s} \tag{5}$$

(Carslaw & Jaeger 1986), where $\kappa_s$ is the thermal diffusivity of the solid and $z$ is measured in the frame of reference of the moving interface. Next, we observe that, in the typical time given by (3), heat is conducted to the interface from a fluid layer of thickness

$$h_T \sim (\kappa_f \tau)^{1/2} \sim \left(\frac{P\mu_m \kappa_f^2}{gV(\rho_f - \rho_m)}\right)^{1/4}, \tag{6}$$

where $\kappa_f$ is the thermal diffusivity of the fluid. For the moment I shall assume that

$$h_T \gg h_m k_f/k_m, \tag{7}$$

where $k_f$ and $k_m$ are the respective thermal conductivities of the fluid and of the melt, so that an accurate estimate of the heat flux from the fluid to the interface is

$$F \approx k_f(T_f - T_m)/h_T. \tag{8}$$

The heat flux $F$ is linked to the melting rate $V$ by the interfacial condition

$$F = V(\rho_s L_s + \rho_s c_s(T_m - T_s)), \tag{9}$$

where $\rho_s$, $L_s$ and $c_s$ are the density, latent heat and specific heat of the solid. Substitution of (6) and (8) into (9) yields the prediction that the melting velocity is

$$V \sim \left(\frac{g(\rho_f - \rho_m)\kappa_f^2}{P\mu_m \mathscr{S}^4}\right)^{1/3}, \tag{10}$$

where the Stefan number $\mathscr{S}$ is defined by

$$\mathscr{S} = \frac{\rho_s L_s + \rho_s c_s(T_m - T_s)}{\rho_f c_f(T_f - T_m)}. \tag{11}$$

Using (10), $\tau$ and $h_m$ can be estimated from (3) and (4) as

$$\tau \sim \left(\frac{P^2\mu_m^2 \mathscr{S}^2}{g^2(\rho_f - \rho_m)^2 \kappa_f}\right)^{1/3} \tag{12}$$

and

$$h_m \sim \left(\frac{P\mu_m \kappa_f}{g(\rho_f - \rho_m)\mathscr{S}^2}\right)^{1/3}. \tag{13}$$

It can then be shown that our assumption that compositional diffusion can be neglected in the compositional boundary layer, which requires that $\tau \ll h_m^2/D$ where $D$ is the compositional diffusivity, is satisfied if

$$\mathscr{S} \ll (\kappa_f/D)^{1/2}. \tag{14}$$

In dimensional terms, (14) is equivalent to

$$T_f - T_m \gg \frac{\rho_s L_s + \rho_s c_s(T_m - T_s)}{\rho_f c_f}\left(\frac{D}{\kappa_f}\right)^{1/2}, \tag{15}$$

a quantitative result that is consistent with the conclusion by Woods (1992) that a sufficiently large superheat is required for melting to occur rather than dissolving. A scaling analysis of this transition between melting and dissolving is given in Kerr (1994, Appendix).

Using (13), it can also be shown that the assumption expressed by (7) is equivalent to $\mathscr{S} \gg k_f/k_m$, which is not surprising since the latent heat to form a melt layer of thickness $h_m$ is derived from the overlying fluid layer of thickness $h_T$. For somewhat smaller $\mathscr{S}$ ($\gtrsim k_f/k_m$), $h_m$ cannot be neglected in comparison with $h_T$ in estimating $F$, and $F$ and $V$ are more accurately given by

$$F \approx \frac{T_f - T_m}{(h_T/k_f) + (h_m/k_m)} = \frac{k_f(T_f - T_m)}{h_T}\left(1 + \frac{k_f}{k_m \mathscr{S}}\right)^{-1} \tag{16}$$

and

$$V \propto \mathscr{V} \equiv \left(\frac{g(\rho_f - \rho_m)\kappa_f^2}{P\mu_m \mathscr{S}^4}\right)^{1/3}\left(1 + \frac{k_f}{k_m \mathscr{S}}\right)^{-1}. \tag{17}$$

Finally, if $\mathscr{S} \ll k_f/k_m$, then the temperature profile is very nonlinear, equation (16) is no longer accurate, and a new scaling analysis is required (see Appendix A).

## 3. Experiments

To test the scaling analysis presented in §2, several series of experiments were performed. In all the experiments, the Stefan number lay in the range ($k_f/k_m \lesssim \mathscr{S} \lesssim (\kappa_f/D)^{1/2}$) appropriate for (17).

### 3.1. *Wax floor (WF)*

These experiments were conducted in a Perspex tank that consisted of a lower slot, $19.5 \times 3$ cm$^2$ in cross-section and 20 cm in depth, joined at its top into the base of a much larger region, $19.5 \times 40$ cm$^2$ in cross-section and 30 cm in depth (figure 3). The purpose of this larger region was to provide such a large volume of hot overlying fluid that its temperature and composition would not change significantly during the course of an experiment (in contrast to the experiments of Campbell 1986, Huppert & Sparks 1988*a* and Woods 1991). The wax used was a water-soluble polyethylene glycol wax (PEG 600) that melts at about 18.5 °C. The molten wax was first poured into the experimental tank until the lower slot was half full, and then solidified by immersing the slot in a cold alcohol bath.

The experiments were started using the following procedure. First, the remainder of the slot overlying the wax was filled with cold water. A wire mesh with 2 mm openings was then placed over the slot. Finally, a hot aqueous solution of $NaNO_3$ was rapidly added to the upper region, and the mesh removed. This careful procedure ensured that the wax was not rapidly and unevenly eroded by large-scale forced circulation during the input of the hot overlying solution.

Direct observations of the experiments were supplemented by both photographs and videos. Figure 4 shows a photograph of the flat melting wax interface with plumes of buoyant wax streaming away from it. This observation of vigorous compositional convection reflects the fact that the unstable compositional buoyancy of the melt was always much greater than the stabilizing thermal buoyancy due to the heat that must be removed from the fluid to produce this melt, i.e. the ratio $\mathscr{R}$ of the buoyancies satisfies the condition

$$\mathscr{R} \equiv \frac{\rho_f - \rho_m}{\alpha(\rho_s L_s + \rho_s c_s(T_m - T_s))/c_f} \gg 1, \tag{18}$$

where $\alpha$ is the coefficient of thermal expansion.

Observations of the thickness of the wax block as a function of time demonstrated that the block melted at a constant velocity (figure 5). Such a constant velocity is expected given the almost constant temperature and composition of the overlying fluid. The melting velocities are listed in table 1, together with the Stefan number $\mathscr{S}$ and the velocity scale $\mathscr{V}$ given by (17). The velocities are plotted against $\mathscr{V}$ in figure 6.

### 3.2. *Wax roof (WR)*

The apparatus and techniques for these experiments were similar to those used by Huppert & Sparks (1988*b*). A block of PEG 600 wax, $20 \times 20$ cm$^2$ in cross-section and 7 cm thick, was made inside a Perspex tank with a metal base through which cold fluid was pumped. The Perspex walls were then removed and the wax block inserted into the top of an insulated glass tank to leave a space underneath that was $20 \times 20$ cm$^2$ in cross-section and 53 cm high. The distilled water used as the hot fluid was then added through a hole in the base of the tank until it came in contact with the wax. This contact was maintained throughout the experiments, despite the slight decrease in volume of the fluid as it cooled, by regular small additions of fluid.

Like the WF experiments, these experiments easily satisfied (18) and so the melting

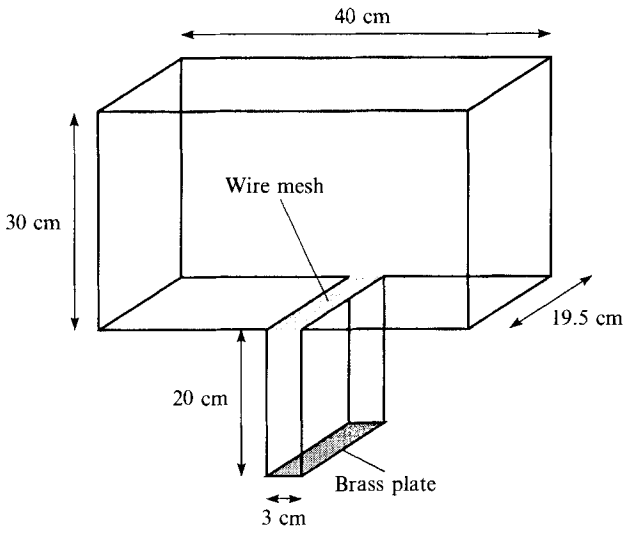


FIGURE 3. Sketch of the Perspex tank used for floor-melting experiments.

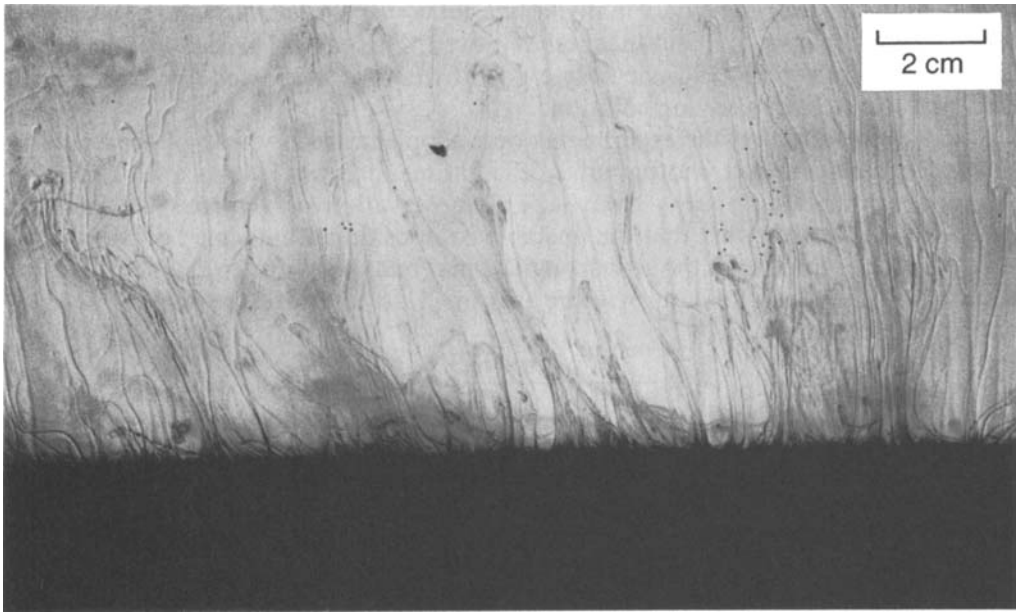


FIGURE 4. Photograph of a wax floor that is melting owing to being overlain by a hot dense aqueous solution of $NaNO_3$.

was driven by compositional convection. The melting velocities, given in table 1, are plotted against the velocity scale $\mathscr{V}$ in figure 6. It is seen that the WR and WF data are consistent, which reflects the fact that the very weak thermal buoyancy (whether positive or negative) played no role in the melting in these experiments. In addition, the collapse of the data onto a straight line supports the scaling analysis that leads to (17).

Finally, the WR experiments can be contrasted with those of Huppert & Sparks (1988*b*). In their experiment 7, the densities of the fluid and wax were carefully matched. The melting was therefore entirely driven by thermal convection and can be accurately predicted using semi-empirical expressions for convective heat transfer (see

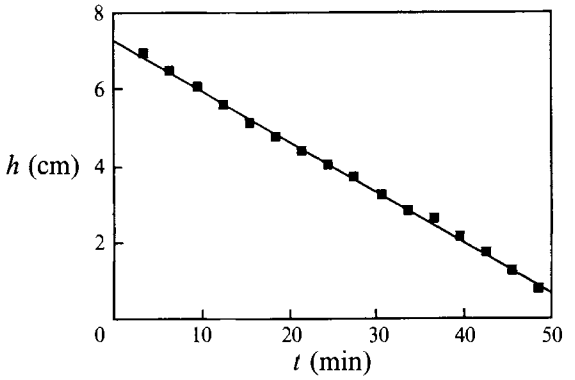


FIGURE 5. The thickness $h$ of the wax block versus time during experiment WF2. The results show that the melting velocity is constant throughout the experiment.

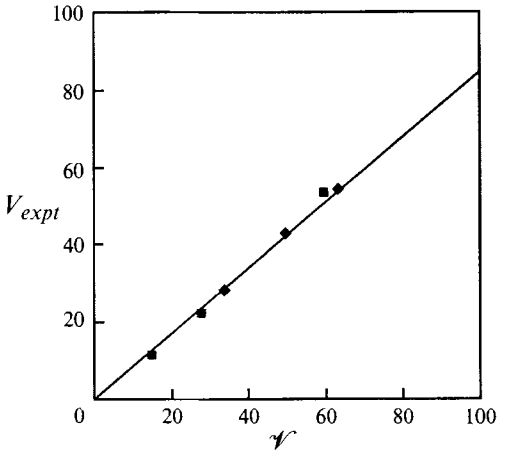


FIGURE 6. The melting velocities (in $\mu$m s$^{-1}$) observed for both a wax floor (■) and a wax roof (◆), in comparison with the velocity scale $\mathscr{V}$ defined by (17). The collapse of the data onto a straight line supports (17), and gives an estimate of the constant of proportionality in (17) of about 0.85.

their figure 5(*a*). In their experiment 8, the wax is denser than the fluid and the melting is therefore driven by both thermal and compositional convection. The thermal buoyancy flux is however dominant ($\mathscr{R} \approx 0.5$), so that the melting is dominated by thermal convection, although it is clear from their figure 5(*b*) that the compositional convection in this case has significantly enhanced the rate of melting.

### 3.3. *Ice roof (IR)*

These experiments used the same apparatus and techniques as the WR experiments described in §3.2. The experiments used aqueous solutions of ethanol, and ice blocks that were free of air bubbles. These crystal-clear blocks were made by using the counter-intuitive technique of bubbling air through the distilled water as it was freezing! This approach, well-known to ice manufacturers, probably works because the bubble-driven convection keeps the water well-mixed and thereby prevents it from becoming heavily supersaturated in air near the water–ice interface (Carte 1961).

The importance of having ice blocks that were free of air bubbles is demonstrated by figure 7, which shows the conical cavities that developed in an experiment due to the presence of a few air bubbles. This phenomenon was not observed for the purely

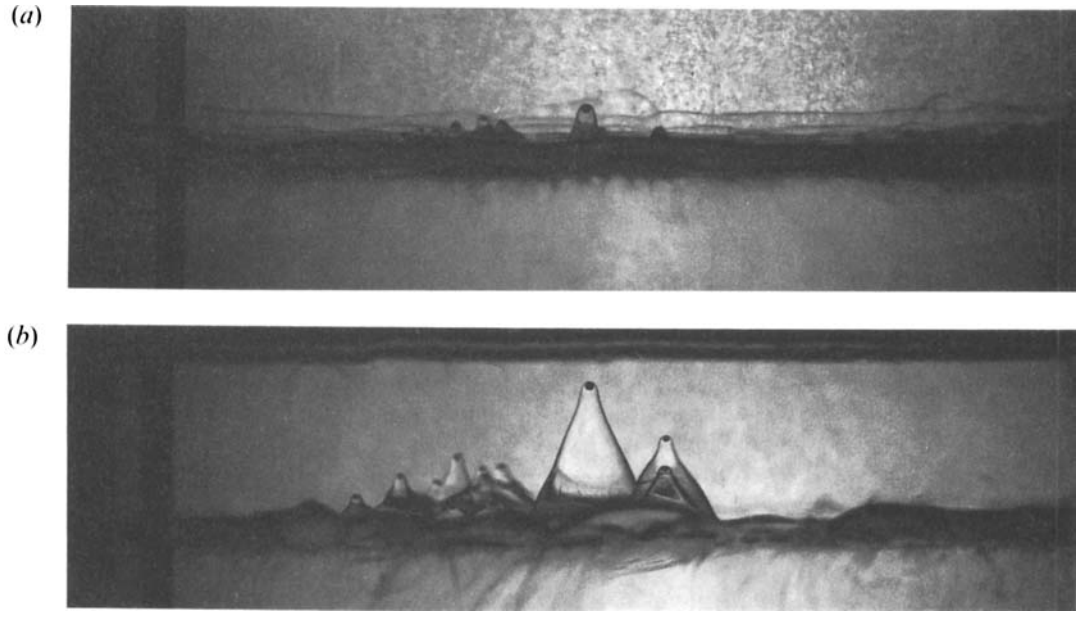


FIGURE 7. Photographs which show the cavities that developed due to the presence of air bubbles when an ice roof melted in contact with an aqueous solution of 36 wt % ethanol with a temperature of about 30 °C. In the time between the photographs (*a*) and (*b*) the interface has melted back about 9 mm.

| Expt | $T_s$ (°C) | $T_f$ (°C) | $\rho_f$ (g cm$^{-3}$) | $\mathscr{S}$ | $V_{expt}$ (μm s$^{-1}$) | $\mathscr{V}$ (μm s$^{-1}$) |
|---|---|---|---|---|---|---|
| WF1 | 7.9 | 44.0 | 1.342 | 2.05 | 53.8 | 59.3 |
| WF2 | 7.9 | 29.5 | 1.346 | 4.75 | 22.2 | 27.5 |
| WF3 | 7.9 | 24.65 | 1.343 | 8.50 | 11.4 | 14.6 |
| WR1 | 3.0 | 35.1 | 0.994 | 3.22 | 28.3 | 33.6 |
| WR2 | 5.0 | 43.9 | 0.990 | 2.05 | 43.0 | 49.3 |
| WR3 | 4.0 | 54.1 | 0.986 | 1.48 | 54.7 | 62.9 |

TABLE 1. Experimental parameters and results for the melting of a wax floor or a wax roof. The parameters $\mathscr{S}$ and $\mathscr{V}$ are defined by (11) and (17) respectively. The calculations use the following values of the thermophysical properties of the PEG 600 wax: $\rho_m = 1.128$ g cm$^{-3}$, $\mu_m = 1.8$ g cm$^{-1}$ s$^{-1}$, $\kappa_m = 0.8 \pm 0.1 \times 10^{-3}$ cm$^2$ s$^{-1}$, $k_m = 0.0024$ J s$^{-1}$ cm$^{-1}$ K$^{-1}$, $\rho_s = 1.21$ g cm$^{-3}$, $L_s = 146$ J g$^{-1}$ and $c_s = 2.49$ J g$^{-1}$ °C$^{-1}$ (obtained from direct laboratory measurement and from Fink & Griffiths (1990, and personal communication)). The WF experiments used aqueous solutions of $NaNO_3$ while the WR experiments used distilled water; the physical properties of these fluids as a function of temperature and concentration were determined from tabulations by Washburn (1926) and Weast (1989). The values of $V_{expt}$ and $\mathscr{V}$ are believed accurate to within about 5% and 10%, respectively.

thermally driven melting of an ice roof in contact with hot water (the interface in this case had gentle undulations with an amplitude of less than 1 mm), but became more dramatic and problematic as the alcohol content of the fluid was increased.

During the experiments, there was a significant decrease in the fluid temperature, and hence also in the melting rate. These quantities were therefore evaluated, at a time about half-way through an experiment, from quadratic least-squares fits to

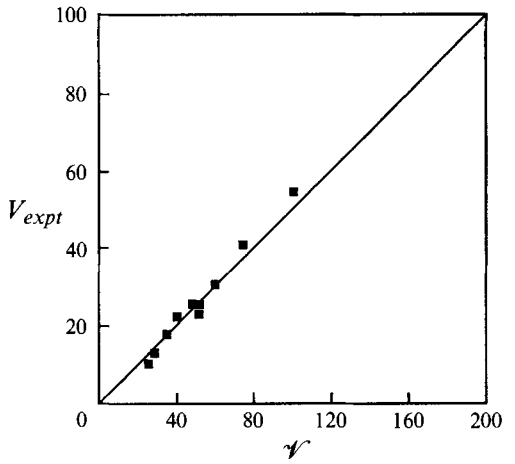


FIGURE 8. The melting velocities (in μm $s^{-1}$) of an ice roof, in comparison with the velocity scale $\mathscr{V}$ defined by (17). The experiments collapse onto a straight line, in agreement with (17), with a constant of proportionality of about 0.50.

| Expt | $T_s$ (°C) | $T_f$ (°C) | $\rho_f$ (g $cm^{-3}$) | $\mathscr{S}$ | $V_{expt}$ (μm $s^{-1}$) | $\mathscr{V}$ ( m $s^{-1}$) |
|---|---|---|---|---|---|---|
| IR1 | −7 | 17.7 | 0.995 | 4.26 | 23.2 | 41.3 |
| IR2 | −7 | 18.0 | 0.988 | 4.18 | 25.8 | 53.8 |
| IR3 | −7 | 9.25 | 0.985 | 8.17 | 10.7 | 26.2 |
| IR4 | −7 | 10.2 | 0.973 | 7.73 | 13.6 | 30.2 |
| IR5 | −7 | 28.3 | 0.970 | 2.83 | 56.7 | 102.3 |
| IR6 | −7 | 16.2 | 0.964 | 5.05 | 23.8 | 53.2 |
| IR7 | −7 | 12.1 | 0.946 | 7.60 | 18.8 | 36.2 |
| IR8 | −7 | 22.4 | 0.928 | 4.48 | 42.5 | 77.0 |
| IR9 | −7 | 16.3 | 0.888 | 7.38 | 25.7 | 49.3 |
| IR10 | −7 | 20.3 | 0.852 | 6.59 | 31.7 | 61.8 |

TABLE 2. Experimental parameters and results for the melting of an ice roof. $\mathscr{S}$ and $\mathscr{V}$ are defined by (11) and (17) respectively. All the experiments used aqueous solutions of ethanol. In experiment IR1, the ratio of $V_{expt}$ to $\mathscr{V}$ is relatively large because the melting is driven both by the compositional buoyancy and by a comparable thermal buoyancy (i.e. $\mathscr{R} \approx 1$; see Appendix B). The physical properties of the ice, the melt water and the solutions were determined from tabulations by Washburn (1926) and Weast (1989). The values of $V_{expt}$ and $\mathscr{V}$ are accurate to within about 10% and 5%, respectively.

observations of the temperature and interface position as a function of time. These values, given in table 2, are accurate to about 10%. The melting velocities are plotted against the velocity scale $\mathscr{V}$ in figure 8. The two quantities are found to be linearly related, as was found in figure 6 for the wax melting data.

### 3.4. *Ice floor (IF)*

These experiments used the same apparatus and techniques as described in §3.1 for the melting of a wax floor. The experiments, summarized in table 3, covered a wide range in $T_F$, $\rho_f$ and $\mu_f$. The largest value of $T_f$ used was about 40 °C, since higher temperatures lead to thermal expansion stresses that cracked the ice.

All the experiments used aqueous solutions of $K_2CO_3$, except experiment IF19 which used a NaCl solution. The NaCl experiment was chosen to be similar to experiment

| Expt | $T_s$ (°C) | $T_f$ (°C) | $\rho_f$ (g cm$^{-3}$) | $\mathscr{S}$ | $V_{expt}$ (μm s$^{-1}$) | $\mathscr{V}$ (μm s$^{-1}$) |
|---|---|---|---|---|---|---|
| IF1 | −15.0 | 18.9 | 1.395 | 4.56 | 48.8 | 138.5 |
| IF2 | −15.2 | 20.5 | 1.524 | 4.16 | 44.0 | 143.0 |
| IF3 | −17.9 | 29.1 | 1.511 | 2.98 | 66.2 | 211.8 |
| IF4 | −11.0 | 38.0 | 1.493 | 2.20 | 102.2 | 298.5 |
| IF5 | −16.0 | 37.9 | 1.511 | 2.27 | 97.0 | 285.7 |
| IF6 | −16.7 | 19.2 | 1.288 | 4.50 | 48.8 | 138.2 |
| IF7 | −15.6 | 19.5 | 1.188 | 4.33 | 45.7 | 133.2 |
| IF8 | −16.2 | 19.6 | 1.110 | 4.25 | 39.5 | 118.3 |
| IF9 | −10.0 | 19.6 | 1.073 | 4.06 | 27.5 | 109.7 |
| IF10 | −21.6 | 19.0 | 1.089 | 4.48 | 28.5 | 104.2 |
| IF11 | −19.1 | 33.3 | 1.486 | 2.63 | 90.5 | 248.3 |
| IF12 | −18.1 | 16.9 | 1.422 | 5.18 | 38.7 | 118.2 |
| IF13 | −19.5 | 25.4 | 1.390 | 3.47 | 66.7 | 189.7 |
| IF14 | −17.3 | 11.6 | 1.116 | 7.23 | 19.8 | 63.8 |
| IF15 | −19.9 | 15.0 | 1.279 | 5.85 | 33.5 | 100.7 |
| IF16 | −18.4 | 13.5 | 1.197 | 6.37 | 27.8 | 85.3 |
| IF17 | −18.7 | 8.3 | 1.119 | 10.19 | 13.2 | 42.0 |
| IF18 | −16.7 | 9.4 | 1.095 | 8.84 | 13.9 | 46.8 |
| IF19 | −20.7 | 18.7 | 1.165 | 4.70 | 39.8 | 117.0 |
| IF20 | −10.7 | 14.8 | 1.482 | 5.66 | 37.3 | 102.8 |
| IF21 | −15.1 | 9.5 | 1.508 | 9.00 | 23.5 | 56.8 |
| IF22 | −18.7 | 11.1 | 1.502 | 7.86 | 27.5 | 67.7 |
| IF23 | −18.2 | 9.7 | 1.465 | 9.01 | 23.3 | 58.7 |
| IF24 | −19.2 | 7.9 | 1.454 | 11.13 | 19.8 | 45.3 |
| IF25 | −18.8 | 13.4 | 1.439 | 6.55 | 30.7 | 88.3 |
| IF26 | −18.6 | 11.0 | 1.291 | 7.94 | 25.7 | 69.8 |
| IF27 | −19.4 | 9.2 | 1.204 | 9.41 | 19.8 | 53.2 |
| IF28 | −8.5 | 5.45 | 1.111 | 14.63 | 11.2 | 26.0 |
| IF29 | −19.6 | 20.0 | 1.036 | | | |
| IF30 | −21.1 | 20.0 | 1.057 | | | |
| IF31 | −20.0 | 20.1 | 1.064 | | | |
| IF32 | −15.8 | 19.5 | 1.071 | | | |
| IF33 | −18.6 | 7.0 | 1.078 | | | |
| IF34 | −13.0 | 40.1 | 1.065 | | | |
| IF35 | −17.1 | 6.6 | 1.101 | | | |

TABLE 3. Experimental parameters and results for the melting of an ice floor; the experiments are divided into those (IF1–19) that produced a flat interface, those (IF20–28) that produced a pitted interface, and those (IF29–35) where the melting velocity decreased rapidly with time. $\mathscr{S}$ and $\mathscr{V}$ are defined by (11) and (17) respectively. All the experiments used aqueous solutions of $K_2CO_3$ except experiment IF19 which used a NaCl solution. The physical properties of the ice, the melt water and the solutions were determined from tabulations by Washburn (1926) and Weast (1989). The values of $V_{expt}$ and $\mathscr{V}$ are accurate to within about 7% and 5%, respectively.

IF7, except that the former fluid has a freezing point depression of −19.4 °C while for the latter it is only −8.7 °C. The rates of melting in the two experiments were found to be similar, which confirms the assumption used in §2 that melting is controlled by thermal diffusion and that compositional diffusion can be neglected.

Three different melting regimes were observed in the $K_2CO_3$ experiments and are delineated in figure 9. The first regime (previously observed by both Huppert & Sparks 1988*a*, figure 3, and Woods 1991, figure 3) occurred if the $K_2CO_3$ concentration, and hence the fluid density, was too small. In this case, the compositional buoyancy of the

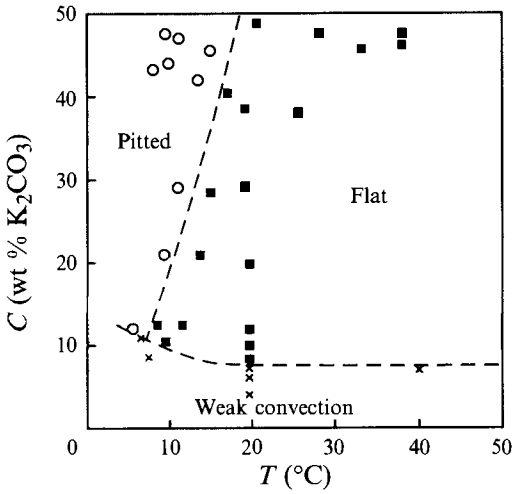


FIGURE 9. The three melting regimes observed in 34 experiments in which aqueous solutions of $K_2CO_3$ melted an ice floor (see table 3): melting at a constant velocity with a flat interface (■), at a constant velocity with a pitted interface (○), or with a rapidly decreasing velocity if the compositional convection is too weak to keep the solution thermally well-mixed (×).

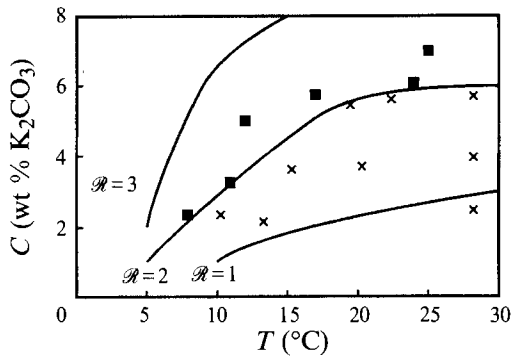


FIGURE 10. Additional experiments in which aqueous solutions of $K_2CO_3$ melted an ice floor with an initial temperature $T_s = -1 \pm 1$ °C. The experiments either melted at a constant velocity (■) or with a rapidly decreasing velocity if the compositional convection is too weak to keep the solution thermally well-mixed (×). Also shown are contours of constant density ratio $\mathscr{R}$, which demonstrates that the boundary between the two convective regimes lies at about $\mathscr{R} = 2.0$.

melt was insufficient to transport the cold dense fluid away from the interface, so that the fluid became thermally stratified and the melting rate decreased rapidly with time. The boundary of this regime was found to lie at about 8 wt% $K_2CO_3$, which corresponds to a value of $\mathscr{R}$ of about 2.6. It was clear however that the precise position of this boundary was affected by an initial transient at the start of the experiments where the supercooled solid adjusted to the melting temperature at the boundary. Some further experiments were therefore performed in which the initial temperature of the ice was only slightly below its melting point. The results of these experiments, summarized in figure 10, indicate a critical value $\mathscr{R}_c$ of about 2.0, which therefore implies that the energetic efficiency with which the buoyant melt water can carry away the cold dense fluid is about 50%. It should also be noted that $\mathscr{R}_c$ is probably a function

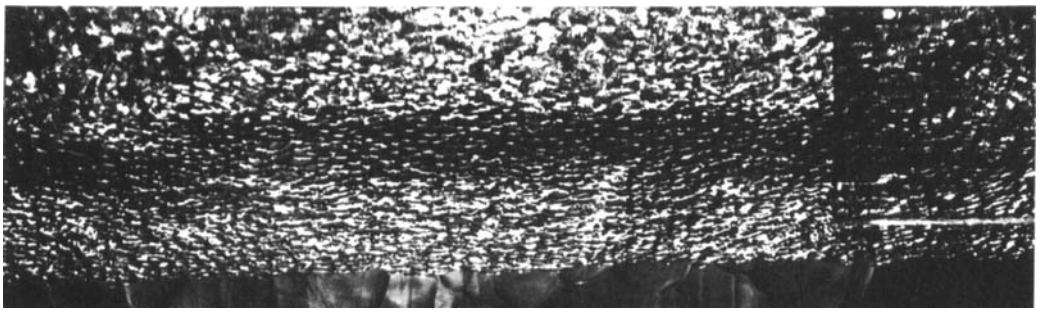

FIGURE 11. Photograph which shows an example of the pitted surface of the melting ice seen during experiments IF20–28. The ruler markings are in mm.

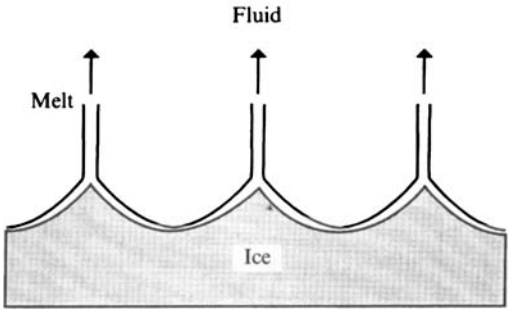


FIGURE 12. Schematic diagram which indicates the convective flow of the buoyant melt water when the ice interface was pitted.

of the viscosity ratio $\mu_f/\mu_m$: the above critical value has been obtained from experiments in which these viscosities are comparable, and it seems likely that $\mathscr{R}_c$ will be higher for unequal viscosities since the viscous coupling between the melt and fluid should then be reduced.

In both the other two regimes indicated in figure 9, the melting was driven by vigorous compositional convection and occurred at a fixed velocity. What distinguished these two regimes was the nature of the ice interface, which was flat (as discerned by the naked eye) for large enough fluid temperatures, but which became increasingly pitted as $T_f$ was decreased. The pits, shown in figure 11, have been previously observed by Campbell (1986, figure 7) and by Fang & Hellawell (1988, figure 3). The buoyant melt water released in the middle of a pit was observed to flow laterally until it detached from the interface at cusps which separated the pits (see figure 12).

The typical width of the pits in IF20–28 was 1–2 mm, and can be compared with the typical values of the lengthscales $h_T$ (estimated from (8) and (9) as about 0.5 mm), $h_m$ (given by $h_T/\mathscr{S}$ as about 0.05–0.09 mm) and $\lambda$ (found from (1) and (2) as 0.3–0.6 mm). In particular, it is noticeable that the width of the pits is somewhat larger than $\lambda$, an observation that suggests that nonlinear (finite-amplitude) effects may be important in the formation of the pits.

The melting velocities, which are accurate to about 7%, are plotted against the velocity scale $\mathscr{V}$ in figure 13. The data are again found to lie on a straight line,

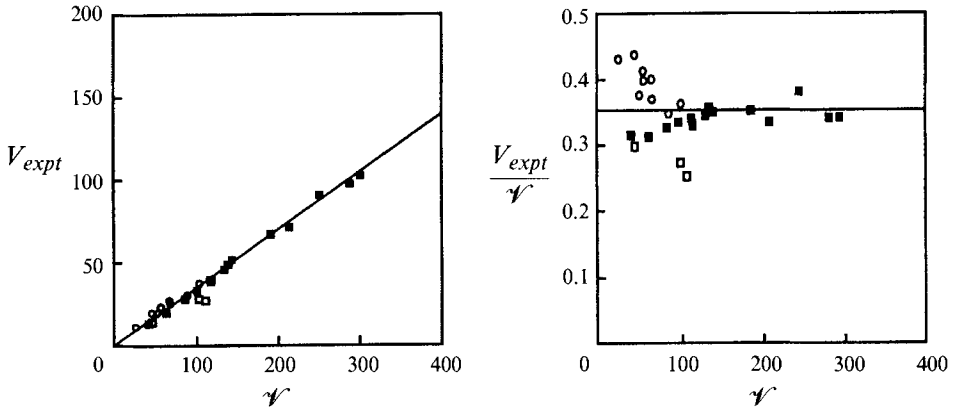


FIGURE 13. The melting velocities (in $\mu$m s$^{-1}$) observed for an ice floor, in comparison with the velocity scale $\mathscr{V}$ defined by (17). In the three experiments denoted by □ (IF9, IF10, IF18, in table 3), the stabilizing thermal buoyancy is not quite large enough to prevent melting at a fixed velocity but is sufficient to weaken the compositional convection significantly and hence to reduce the melting velocity. The remaining 16 experiments that yielded a flat interface (■) collapse onto a straight line, in agreement with (17), with a constant of proportionality of about 0.35. The melting velocities of the experiments that produced a pitted interface (○) are found to be somewhat faster than that predicted for a flat interface; this increased velocity may be due to the larger surface area of the pitted interface which may enhance the diffusion of heat to it.

consistent with (17), although it is clear from the figure that the melting rate was reduced in a few experiments where the negative thermal buoyancy was significant. The figure also shows that the melting rate was larger in the experiments that produced pits. This result may reflect an enhanced thermal transport to the pitted interface due to its larger surface area. As an additional explanation, it is also noted that, in experiments such as IF24 and IF28 where the Stefan number approaches $(\kappa_f/D)^{1/2} \approx 15$, compositional diffusion will significantly enhance melting by producing an interfacial temperature that is less than $T_m$ (see Kerr 1994, Appendix).

### 3.5. *Sloping ice floor*

These experiments were similar to those summarized in figure 10, except that the ice floor was inclined at 30° to the horizontal. Like the experiments on a horizontal floor, the experiments on a sloping floor revealed the existence of two convective regimes. When $\mathscr{R}$ was sufficiently large, a regime of vigorous compositional convection was observed, in which the solution remained well-mixed (figure 14) and the surface of the ice was cusped (as shown in figure 11). In contrast, for sufficiently small $\mathscr{R}$, the compositional convection was unable to keep the fluid well-mixed, and it became increasingly thermally stratified as cold fluid flowed down the ice and ponded at the base of the tank (figure 15). The thermal downflow and simultaneous compositional convection resulted in an ice surface that consisted of a series of parallel grooves running down the slope (figure 16). The critical value $\mathscr{R}_c$ separating these two regimes was found to be about 2.7 (see figure 17). This value is larger than the value of about 2.0 found for a horizontal ice floor, a result which suggests that the mixing efficiency of the compositional convection is hindered by the downslope flow in the thermal boundary layer. It is therefore anticipated that $\mathscr{R}_c$ is a monotonically increasing function of the slope of the floor.

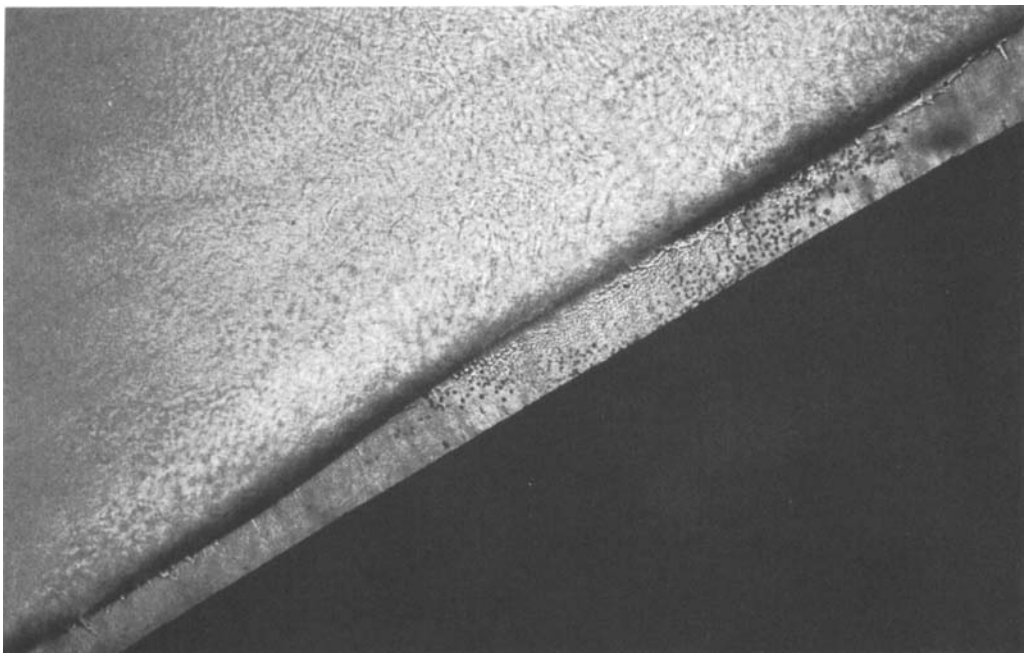

FIGURE 14. Shadowgraph showing the vigorous compositional convection that occurred for $\mathscr{R} = 3.3$ during the melting of a sloping ice floor. The motion is very similar to the vigorous thermal convection from a sloping floor that was studied by Martin & Campbell (1988).

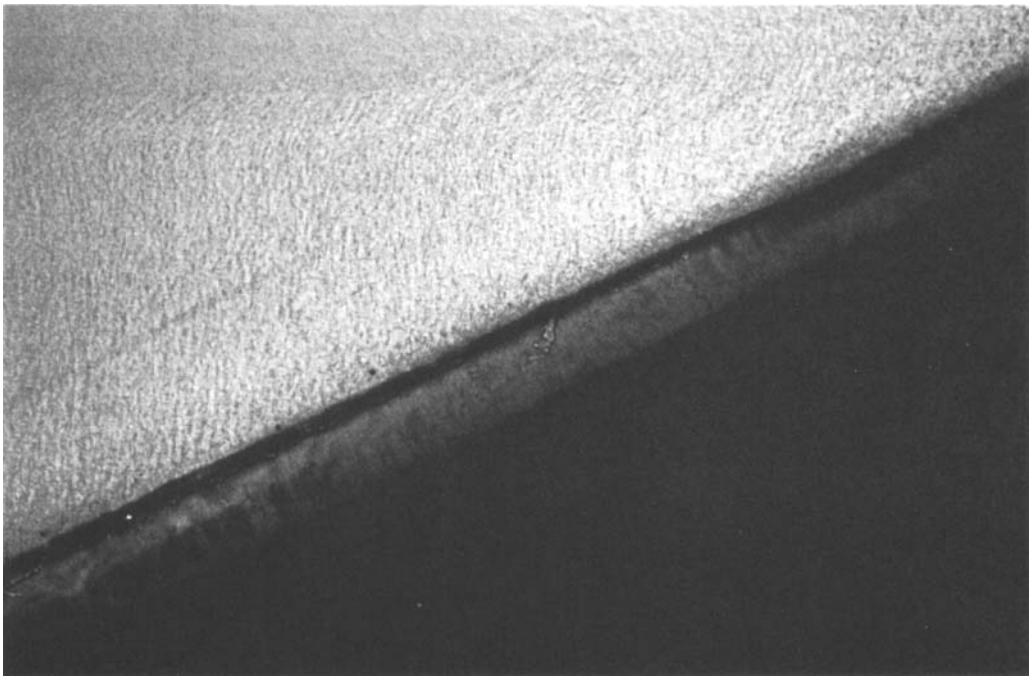

FIGURE 15. Shadowgraph showing the thermal stratification that developed after eight minutes of an experiment (with $\mathscr{R} = 1.7$) in which the compositional convection was too weak to keep the solution well-mixed. The thermal stratification by this time has reached the top of the ice block, and is indicated by the vertical nature of weak compositionally buoyant plumes leaving the slowly melting ice.

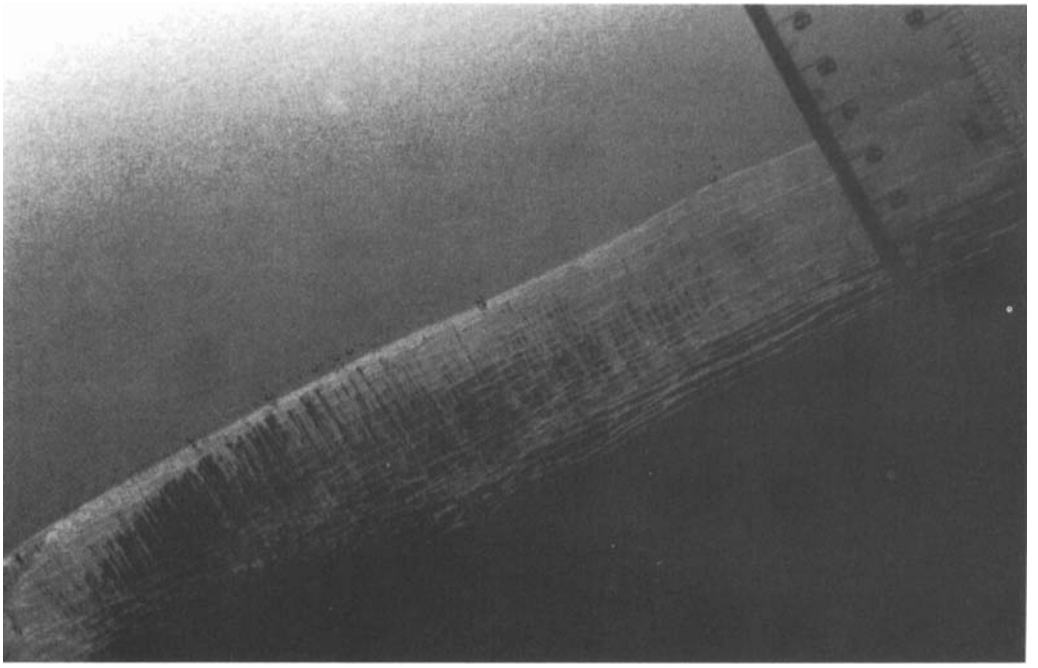

FIGURE 16. Photograph of the grooves in the sloping ice surface which formed (with $\mathscr{R} = 1.6$) during an experiment that became thermally stratified.

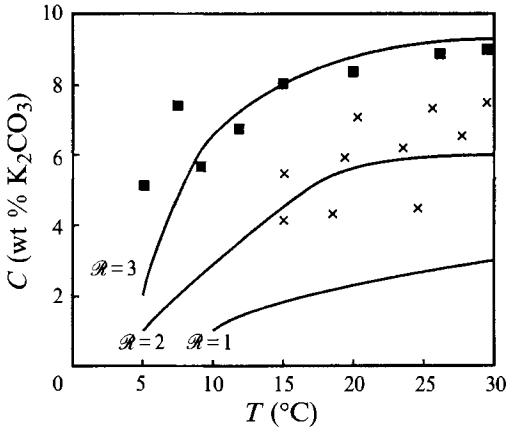


FIGURE 17. A summary of the behaviour of a series of experiments in which aqueous solutions of $K_2CO_3$ melted an ice floor that was inclined at 30° to the horizontal. The ice had an initial temperature $T_s = -2 \pm 2$ °C. The solution in the experiments either remained well-mixed (■) or rapidly became thermally stratified if the compositional convection was too weak ( × ). Also shown are contours of constant density ratio $\mathscr{R}$, which demonstrates that the boundary between the two convective regimes lies at about $\mathscr{R} = 2.7$.

## 4. Discussion

### 4.1. *Melting velocities*

One surprising result of the experiments described in §§3.1–3.4 is that although each series of experiments supported (17) the experiments yielded different values of the constant of proportionality in this scaling relationship (see table 4). The differences in these values are much larger than either the error in determining experimentally $V_{expt}$ or the error in evaluating $\mathscr{V}$ due to uncertainties in the physical properties of the solids and fluids.

A plausible explanation of this variation may lie in the different *heats of solution* released as the melt and fluid mix. The significance of the heat of solution is suggested by the observation that while the fluid temperature decreased significantly in the ice-roof experiments, it decreased only slightly during the evolution of the wax-roof experiments, which implies that the heat of solution in the latter case must be large and comparable to the latent heat of the wax. Table 4 gives the measured heats of solution for the experiments, and suggests that the value of the melting constant increases as the heat of solution is increased; this result seems physically reasonable because any heat released by mixing of the melt and fluid in the vicinity of the interface would increase the heat transfer to the interface and hence the melting velocity.

### 4.2. *Ice pits*

One interesting feature of the ice melting experiments was the formation of pits in some of the IF experiments. Such pits were not observed in any of the IR experiments, which suggests that the formation of pits may require the presence of a stable thermal boundary layer in addition to the unstable compositional boundary layer. The interaction of these boundary layers is likely to depend on their relative thicknesses, viscosities and buoyancies, and hence on the parameters $\mathscr{S}$, $\mu_f/\mu_m$ and $\mathscr{R}$. Figure 9 indicates that the pits became apparent at small temperatures (large $\mathscr{S}$), and were favoured by large concentrations of $K_2CO_3$ (which corresponds to simultaneously large values of both $\mu_f/\mu_m$ and $\mathscr{R}$). The formation of pits may also depend on the vigour of the compositional convection in the overlying fluid (and hence on the depth of this fluid), and on the temperature gradient immediately ahead of the melting interface, which from (5) is given by

$$\left.\frac{\mathrm{d}T}{\mathrm{d}z}\right|_{z=0^+} = -\frac{V}{\kappa_s}(T_m - T_s). \tag{19}$$

It is also interesting to note that pits were not observed in the WF experiments. This might reflect the high viscosity of the wax ($\mu_m \gg \mu_f$), which may buffer the interface from the overlying convection. Alternatively, the formation or observation of pits may be prevented by the range in molecular weights of the polyethylene glycol composing the wax, which cause it to melt over a range of temperatures (in contrast to the sharp melting point of 0 °C for ice).

### 4.3. *Ice cavities*

An intriguing observation in some of the IR experiments was the formation by air bubbles of cavities in the ice. For example, several cavities developed in IR10; in this case, the melting velocity at the top of cavities was about two and a half times greater than the melting velocity of the otherwise-flat interface.

In contrast to the IR experiments where melting is driven by both thermal and compositional convection, no such cavities form when ice melts above hot water: in this case, the interface remains very flat and any bubbles migrate freely over the surface

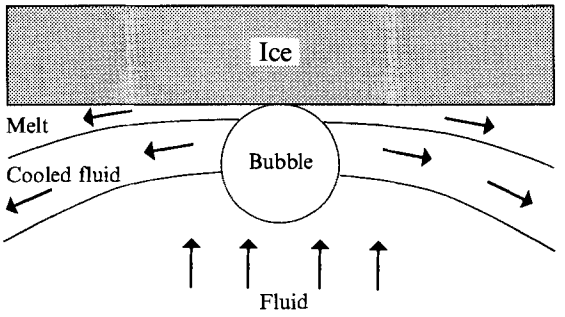


FIGURE 18. Schematic diagram which illustrates the convective flow that seems necessary for a bubble to be able to induce cavities to form in the melting ice (see the discussion in §4.3).

| Expt | Constant in (17) | Heat of solution ($J\ g^{-1}$) |
|---|---|---|
| WR | 0.85 | 145 |
| WF | 0.85 | 107 |
| IR | 0.50 | 0–60 |
| IF | 0.35 | $\approx 0$ |

TABLE 4. Values of the constant in (17) inferred from the different series of experiments in §3 (see figures 6, 8 and 13), together with the measured heats of solution for mixing of the melt and fluid. The heats of solution were determined from measurements of the increase in temperature of the fluid as known weights of melt were mixed with it, and are accurate to about 10%. In the ice roof series of experiments, the heat of solution increased as the ethanol concentration in the aqueous solutions increased.

as it melts. This result is to be expected since the lower thermal conductivity of the air should reduce melting in the vicinity of the bubble, so that it should soon lie against a bump in the interface from which it can be easily displaced laterally by the vigorous underlying thermal convection.

The cavity instability must therefore be associated with the presence of a compositional boundary layer, and must be driven by a convective flow that is sufficiently strong that it can actually enhance heat transfer and melting in the vicinity of the air bubble. One way this situation might be achieved is if the bubble is able to prevent instability of the compositional boundary layer in its vicinity, which could lead to a flow field (figure 18) in which the thermal boundary layer is thinnest near the bubble.

It is clear that much further work is required to determine the exact conditions under which this novel instability occurs (e.g. is there a critical alcohol concentration or a critical bubble size needed for instability?) and to explain the finite-amplitude development of the observed cavity shape.

## 5. Geological application

The primary motivation of the current paper stems from a desire to understand the behaviour of large volumes of molten rock that are emplaced in the Earth's continental crust. These magmas, which typically have a basaltic composition, rise through the crust in dykes until they reach a level where they are neutrally buoyant (Ryan 1987; Lister 1990; Lister & Kerr 1991). The crust itself is composed predominantly of silica-

| Parameter | Value | Units |
|---|---|---|
| $\rho_f$ | 2.7 | g cm$^{-3}$ |
| $\rho_m$ | 2.3 | g cm$^{-3}$ |
| $\rho_s$ | 2.7 | g cm$^{-3}$ |
| $\alpha$ | $5\times10^{-5}$ | °C$^{-1}$ |
| $L_s$ | 293 | J g$^{-1}$ |
| $c_s$ | 1.34 | J g$^{-1}$ °C$^{-1}$ |
| $c_f$ | 1.34 | J g$^{-1}$ °C$^{-1}$ |
| $g$ | 981 | cm s$^{-2}$ |
| $T_f$ | 1200 | °C |
| $T_m$ | 850 | °C |
| $T_s$ | 600 | °C |
| $\mu_f$ | $10^3$ | g cm$^{-1}$ s$^{-1}$ |
| $\mu_m$ | $10^7$ | g cm$^{-1}$ s$^{-1}$ |
| $k_f$ | 0.029 | W cm$^{-1}$ °C$^{-1}$ |
| $k_m$ | 0.029 | W cm$^{-1}$ °C$^{-1}$ |
| $\kappa_f$ | 0.008 | cm$^2$ s$^{-1}$ |
| $\mathscr{R}$ | 7.6 | |
| $\mathscr{S}$ | 1.10 | |
| $\mu_f/\mu_m$ | $10^{-4}$ | |

TABLE 5. Parameter values used for a basaltic magma intruded into the continental crust (cf. Huppert & Sparks 1988*c*).

rich rocks that have a lower melting temperature than the basalt. As a result, melting of the surrounding crust can occur both during the rise of the hot basalt (Campbell 1985; Huppert & Sparks 1985; Bruce & Huppert 1989; Philpotts & Asher 1993), and after it has arrived at its level of emplacement (Irvine 1970).

At the roof of a basaltic magma chamber, melting will produce a separate convecting layer of buoyant crustal magma (Campbell & Turner 1987). Quantitative modelling of this process (Huppert & Sparks 1988*b*, *c*) has shown that the cooling and crystallization of a 500 m thick layer of basalt will take about 100 years, and can yield up to 300 m of melted roof. In addition, Huppert & Sparks (1988*a*) also noted that the basalt can simultaneously melt its floor, and Woods (1991) has suggested that floor melting could dominate roof melting. Such floor melting is of particular geological interest because it provides a means of mixing the crustal and basaltic magmas to produce a hybrid magma of intermediate composition. In this section the results from §§2 and 3 are used to examine the extent to which a basaltic magma chamber can melt its floor. Melting of the walls of the chamber, and of crustal blocks that fall into the chamber, are also considered.

### 5.1. *Floor melting without crystallization*

I begin by initially considering only the cooling of the basalt, and for the time being will neglect the effects of crystallization within it. In this simpler case, given typical values of the geological parameters (table 5), the buoyancy ratio $\mathscr{R}$ is about 7.6. Since $\mathscr{R}$ is greater than the critical value of about 2.0, vigorous compositional convection would be expected to occur. Since $\mu_m \gg \mu_f$, $P$ and $Q$ are given by (2*a*), and the melting velocity can then be estimated from the experiments as

$$V = 0.35\left(\frac{g(\rho_f-\rho_m)\,\kappa_f^2}{6.222\mu_m\mathscr{S}^4}\right)^{1/3}\left(1+\frac{k_f}{k_m\mathscr{S}}\right)^{-1}, \tag{20}$$

provided that the heat of solution from mixing of the basaltic and crustal magmas can

be neglected. From (20), a melting velocity of 37.5 m per year is obtained. This value is an order of magnitude greater than the rate at which the roof melts, a result which is due to the compositional buoyancy that drives floor melting being much greater than the thermal buoyancy that drives convective heat transfer and melting at the roof. It is also noted that the melting velocity corresponds (from (9) and (16)) to a thermal-boundary-layer thickness $h_T = 32.1$ cm, a melt-layer thickness $h_m = h_T/\mathscr{S} = 29.1$ cm, a timescale $\tau = h_m/V$ for gravitational instability of the compositional boundary layer of about 2.84 days, and a most-unstable wavelength $\lambda = 86.1$ cm.

### 5.2. *Floor melting with crystallization*

The major weakness in the above estimates is the neglect of the effects of crystallization in the thermal boundary layer. For the centimetre lengthscales predicted above and the imposed temperature differences of hundreds of degrees, Brandeis, Jaupart & Allègre (1984) have shown that magmas will nucleate and grow crystals in times of order 0.01–0.1 days. Since this crystallization time is much less than $\tau$, substantial crystallization is expected in the thermal boundary layer (a similar argument has been given by Brandeis & Jaupart 1986 for the case of cooling, crystallization and convection at the roof of a magma chamber). For a basaltic magma, the crystal fraction as a function of temperature $T$ (in °C) is approximately given by Huppert & Sparks (1988*c*) as

$$x = \frac{7200}{T} - 6. \tag{21}$$

The crystalline assemblage (typically 10–15 wt % olivine, 30–40 wt % clinopyroxene and 50–60 wt % plagioclase (Cox & Mitchell 1988)) will have a mean crystal density $\rho_c$ of about 3.0 g cm$^{-3}$, a mean latent heat $L_c$ of about 418 J g$^{-1}$, and a fractionation density $\rho_{fr}$ (defined by Sparks & Huppert 1984 as the density of the components selectively extracted from the melt to grow the crystals) of about 2.65 g cm$^{-3}$. Incorporating the effects of crystallization therefore results in an effective specific heat

$$c_f^* = c_f - L_c \,\mathrm{d}x/\mathrm{d}T \tag{22}$$

of 3.4–3.7 J g$^{-1}$ °C$^{-1}$, an effective thermal expansion coefficient

$$\alpha^* = \alpha - \frac{\rho_c - \rho_{fr}}{\rho_f}\frac{\mathrm{d}x}{\mathrm{d}T} \tag{23}$$

of $7.0–7.8 \times 10^{-4}$ °C$^{-1}$, and hence an effective Stefan number

$$\mathscr{S}^* = \frac{\rho_s L_s + \rho_s c_s (T_m - T_s)}{\rho_f c_f^* (T_f - T_m)} \tag{24}$$

of 0.48–0.53, and an effective buoyancy ratio

$$\mathscr{R}^* \equiv \frac{\rho_f - \rho_m}{\alpha^*(\rho_s L_s + \rho_s c_s (T_m - T_s))/c_f^*} \tag{25}$$

of 1.12–1.16. Since the value of $\mathscr{R}^*$ is less than the critical value of about 2.0, it is concluded that the growth of dense crystals in the thermal boundary layer will prevent vigorous compositional convection. Like the experiments in figure 10 with $\mathscr{R} < 2.0$, I envisage instead that the buoyant crustal melt will leave behind on the floor a growing layer of the basaltic crystals which will steadily reduce the heat flux to the floor and hence its melting rate. The initial growth of this crystal layer will be due to floor

melting, but eventually it will be due primarily to crystals generated by roof melting that grow in the vigorously convecting basalt until they sediment on the floor (Martin & Nokes 1988, 1989). Since the convective heat transfer to the roof (Huppert & Sparks 1988*b*) will be fast in comparison with heat transfer through the crystal layer to the floor, the basalt will primarily melt its roof rather than its floor. As a consequence, the basalt will experience little contamination from mixing with melts derived from the melting of its floor (a similar view has also been expressed by Campbell & Turner 1987, p. 171).

### 5.3. *Melting a sloping roof*

An important remaining issue is the viability of melting at the walls of the basaltic magma chamber. The walls can be conveniently subdivided into 'sloping floors' and 'sloping roofs'. I shall postpone a discussion of sloping floors until §5.4, and for the moment will consider sloping roofs where melting is not complicated by the deposition of crystals. On a sloping roof, melting will produce an inner upward-flowing boundary layer of viscous crustal magma and an outer thermal boundary layer that drives vigorous thermal convection in the magma chamber. This situation is comparable to that of the formation of a laminar compositional boundary layer due to multicomponent crystallization on a vertical wall of a magma chamber (Nilson, McBirney & Baker 1985), except for the important difference that melting depends only on the diffusion of heat (see §2), in contrast to multicomponent crystallization and dissolution where compositional diffusion is crucial (Woods 1992; Kerr 1994). As a result of this difference, the compositional boundary layer during melting will be much thicker than the few centimetres predicted by Nilson *et al.* (1985) for crystallization on the wall of a magma chamber.

If the temperature difference $\Delta T$ across the thermal boundary layer is assumed to be very small in comparison to $T_f - T_m$, the thickness $h$ of the compositional boundary layer and the melting velocity $V$ are linked by the interfacial heat flux condition (cf. (8) and (9)):

$$(\rho_s L_s + \rho_s c_s (T_m - T_s))\, V = k_m (T_f - T_m)/h. \tag{26}$$

From conservation of mass

$$\mathrm{d}Q/\mathrm{d}z = V, \tag{27}$$

where $Q$ is the flux of melt at a distance $z$ along the slope. Now

$$Q \sim Uh, \tag{28}$$

where $U$ is the characteristic alongslope velocity, while a balance of viscous and buoyancy forces in the melted layer gives

$$\mu_m U/h^2 \sim g \sin\beta(\rho_f - \rho_m), \tag{29}$$

where $\beta$ is the slope of the roof. Combining (26)–(29) shows that, at a distance $H$ along the sloping roof,

$$h = \frac{1}{K}\left(\frac{\mu_m k_m (T_f - T_m) H}{g \sin\beta(\rho_f - \rho_m)(\rho_s L_s + \rho_s c_s (T_m - T_s))}\right)^{1/4}, \tag{30}$$

$$V = K\left(\frac{k_m (T_f - T_m)}{(\rho_s L_s + \rho_s c_s (T_m - T_s))}\right)^{3/4}\left(\frac{g \sin\beta(\rho_f - \rho_m)}{\mu_m H}\right)^{1/4}, \tag{31}$$

and the corresponding interfacial heat flux $F$ is given by

$$F = K\left(\frac{k_m^3 (T_f - T_m)^3 (\rho_s L_s + \rho_s c_s (T_m - T_s))\, g \sin\beta(\rho_f - \rho_m)}{\mu_m H}\right)^{1/4}, \tag{32}$$

where $K$ is a constant whose magnitude depends on strength of viscous coupling between the compositional and thermal boundary layers. In the limit where $\mathscr{R} \gg 1$ and $\mu_m/\mu_f \gg 1$, the viscous drag associated with the thermal convection can be neglected, and $K = 1/\sqrt{2}$.

Using (32), the temperature difference $\Delta T$ across the thermal boundary layer can be found by equating $F$ to the heat flux $F_T$ due to vigorous thermal convection:

$$F_T = Ck_f\left(\frac{g\alpha\rho_f}{\kappa_f\mu_f}\right)^{1/3}\Delta T^{4/3}, \tag{33}$$

where the empirical constant $C$ has a value of about 0.156 (Katsaros *et al.* 1977; Davaille & Jaupart 1993). The resulting value of $\Delta T$ can then be compared with $T_f - T_m$ to determine the accuracy of the initial assumption used in writing (26). It is also noted that (32) can be written in dimensionless terms as $Nu_m = \frac{4}{3}K(\mathscr{S}_m\, Ra_m)^{1/4}$, where the Nusselt number

$$Nu_m = \int_0^H F(z)\,\mathrm{d}z/k_m(T_f - T_m), \tag{34}$$

the Stefan number

$$\mathscr{S}_m = (\rho_s L_s + \rho_s c_s(T_m - T_s))/(\rho_m c_m(T_f - T_m)), \tag{35}$$

the Rayleigh number

$$Ra_m = g\sin\beta(\rho_f - \rho_m)H^3/(\kappa_m\mu_m), \tag{36}$$

and $z$ is the distance upslope. This result is analogous to the $Nu \sim Ra^{1/4}$ expression for laminar convection on a wall (Bird, Stewart & Lightfoot 1960; Turner 1979).

As a test of the scaling analysis presented above, a laboratory experiment was performed in which a sloping wax block was melted in contact with an aqueous solution of NaCl (see figure 19). The melted wax was observed to flow upwards in a thin laminar boundary layer. The thickness of the boundary layer increased with height, consistent with (30), and reached a value of about 3 mm after a distance of 10 cm upslope. Outside this compositional boundary layer, vigorous thermal convection was observed in the NaCl solution (figure 19*b*), but it did not cause significant mixing between the solution and the melted wax. As figure 19(*a*) indicates, the wax block was observed to melt at a rate that decreased with distance upslope. Measurements of the interfacial position as a function of time were taken from a videotape, and showed that the variation in the melting velocity was consistent with the $V \propto H^{-1/4}$ relationship given by (31), to within the measuring accuracy of about 5%. Using the observed melting velocity of 28 $\mu$m s$^{-1}$ at $H = 10$ cm, the temperature difference $\Delta T$ driving thermal convection is estimated to be about 8 °C (which is small in comparison to $T_f - T_m$), the Reynolds number $Re = Uh\rho_m/\mu_m$ of the boundary layer is about 0.05 (consistent with the observation of laminar flow), and $K$ is estimated to have a value of about $0.44 \pm 0.12$ (the large error in estimating $K$ reflecting the large variation with temperature of both $\mu_m$ and $\rho_m$ across the compositional boundary layer). The experimental value of $K$ is somewhat less than the limiting value of $K = 1/\sqrt{2}$, due both to the small temperature drop across the thermal boundary layer that reduces the temperature difference across the melt layer, and to a viscous drag from downflow of the thermal boundary layer that is significant since $\mathscr{R} \approx 2.3$ is not very large.

If the scaling analysis and an assumed value of $K = 1/\sqrt{2}$ are applied to a magma chamber at a distance $H = 500$ m along a roof of slope $\beta = 45°$, a compositional

(*a*)

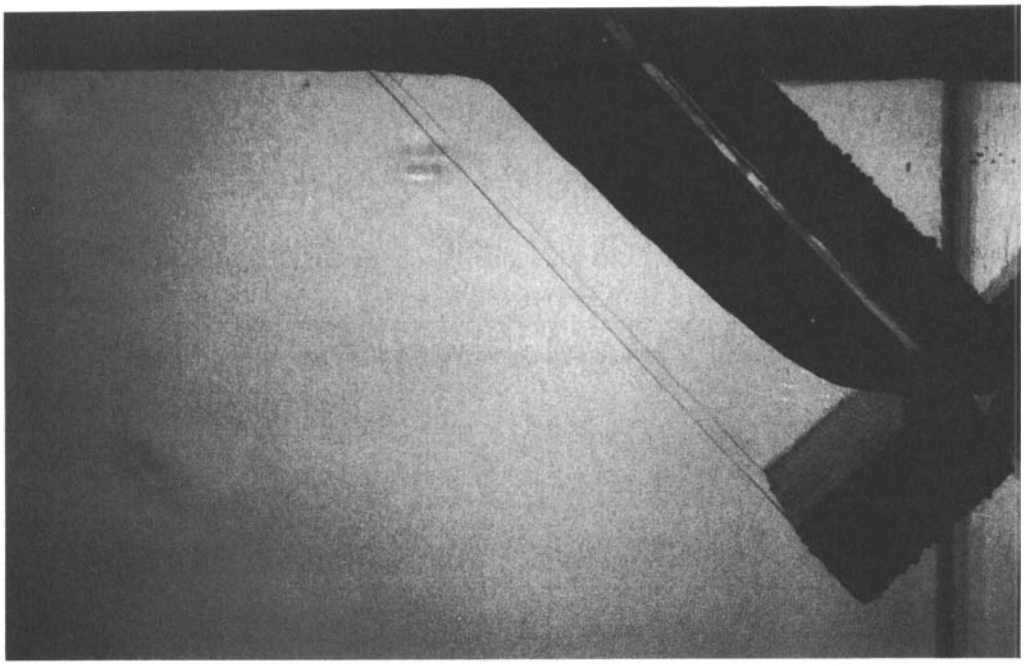

(*b*)

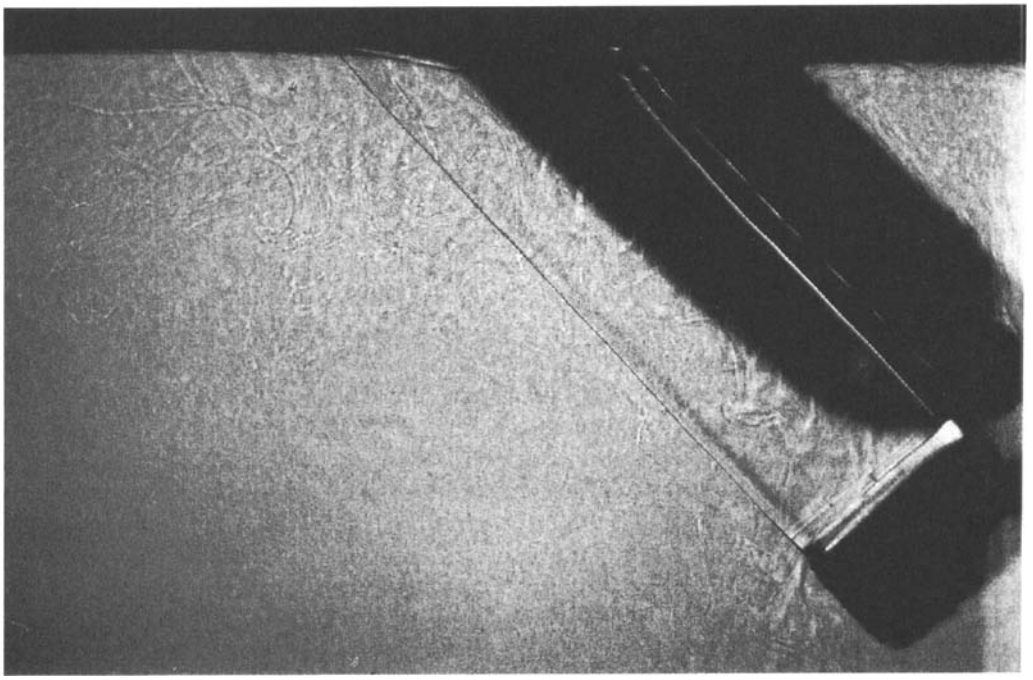

FIGURE 19. Photographs of a sloping wax roof melting in contact with a hot aqueous solution of NaCl. The wax block was 4.5 cm thick, and was contained in a Perspex box whose base and lower wall were insulated with polystyrene. The other experimental conditions were $T_f = 70$ °C, $\rho_f = 1.152$ g cm$^{-3}$, $T_s = 4$ °C and $\beta = 45°$. The experiments were analysed using the following wax

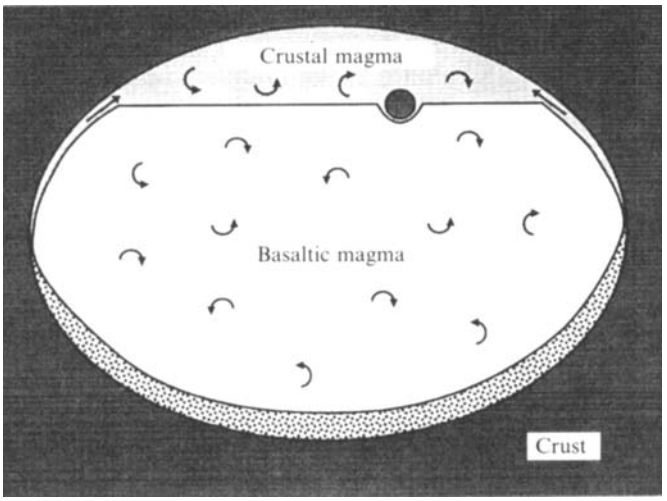


FIGURE 20. Schematic diagram (not to scale) of a convecting basaltic magma chamber that is melting the surrounding continental crust. On the horizontal and sloping floor of the chamber, some melting is expected to occur, but it will be restricted by the growth and deposition of dense crystals (see §§5.2 and 5.4). In contrast, substantial melting is predicted on the horizontal and sloping roof of the chamber. On the sloping parts of the roof, the crustal magma will flow upwards in a laminar boundary layer with little magma mixing (see §5.3). Also sketched at the interface between the two magmas is a melting stoped blocked, about a metre in size, that is being supported by its own buoyant boundary layer (as discussed in §5.5).

boundary layer $h$ of about 0.8 m in thickness, an alongslope velocity $U$ of order 0.05 cm s$^{-1}$, and a melting velocity $V$ of about 23 m per year is predicted. From (33), this melting rate requires a heat flux that can be supplied by thermal convection with a temperature difference $\Delta T$ of about 34 °C (which satisfies the assumption that it is much less than $T_f - T_m$), a thermal-boundary-layer thickness $h_T$ of about 8 cm, a viscous-boundary-layer thickness $h_v \sim 3.2\ (\nu_f/\kappa_f)^{1/2} h_T$ of order 50 m (see Martin & Nokes 1989, equation (A 3)), and mid-chamber r.m.s. convective velocity $V_T \sim (g\alpha \Delta T \kappa_f H/h_T)^{1/3}$ of order 4 cm s$^{-1}$ (see Martin & Nokes 1989, equation (A 8)).

The melting velocity calculated above is significantly larger than the velocities of 3–5 m per year calculated by Huppert & Sparks (1988*b*) for the melting of a horizonal roof. It is therefore concluded that the melting of a sloping roof will be important in any magma chamber in which the sloping roof makes up a significant fraction of the chamber's surface area (see figure 20). The melting of a sloping roof is not expected, however, to result in significant direct mixing between the basaltic and crustal magmas: this conclusion, which is contrary to the suggestion of Campbell & Turner (1987), arises because flow in the compositional boundary layer will be laminar rather than turbulent (since the Reynolds number of the compositional boundary layer $Re \approx 10^{-6}$ is very small, and the interfacial Richardson number $Ri \sim g(\rho_f - \rho_m) h_v/(\rho_f V_T^2) \approx 4 \times 10^4$ is very large).

properties: $\alpha = 0.00083$ °C$^{-1}$ and $\ln(\nu(T)) = 1.7015 - 0.069063T + 0.00031364T^2$, where the respective units of $\nu$ and $T$ are cm$^2$ s$^{-1}$ and °C. (*a*) The wax block after $t = 10$ min. The curvature of the wax interface indicates that the melting velocity decreases with distance upslope, as predicted by (31). (*b*) Shadowgraph showing the vigorous thermal convection in the aqueous solution, which is consistent with the large thermal Rayleigh number ($Ra \approx 10^{10}$).

### 5.4. *Melting a sloping floor*

In the discussion given in §§5.1 and 5.2, the floor of the magma chamber has been considered to be horizontal. While this assumption may be reasonable for many intrusions (e.g. the Bushveld, the Stillwater, and the Pallisades Sill), a number of other intrusions (e.g. the Great Dyke, the Kiglapait, the Muskox, the Jimberlana, and the Fongen-Hyllingen) are funnel-shaped or bowl-shaped, with floor slopes that range up to 90° (Wager & Brown 1968; Campbell 1977; Wilson & Larsen 1985). In this section, we therefore consider the convectively driven melting of sloping floors.

A valuable insight into convection above a sloping floor has been obtained from the thermal convection experiments of Martin & Campbell (1988). They observed that a boundary layer of buoyant fluid grew in thickness with distance upslope until it reached a critical thickness at which it became unstable and broke away from the boundary to drive vigorous convection. Their measurements also showed that the critical boundary-layer thickness on an inclined boundary is identical to that on a horizontal boundary. If this result is applied to floor melting in magma chambers, it is seen from §5.1 that the critical thickness will be about 0.3 m. From (30), it is then found that this critical thickness will be reached at a critical upslope distance $H_c$ of about 10 m. It can therefore be concluded that the region of laminar flow of the compositional boundary layer is negligible in a kilometre-size magma chamber.

As has already been indicated in §5.2, the main limitation on compositional convection will arise from the nucleation and growth dense crystals in the thermal boundary layer. Given the estimate of $\mathscr{R}^* = 1.12$–$1.16$, and the measurements in §3.5 of $\mathscr{R}_c$ for a sloping ice floor, it is clear that the regime of vigorous compositional convection would be prevented by crystal deposition. What is less certain, however, is the behaviour of these dense crystals on a sloping floor.

If the crust is cold or the slope of the floor is small, the growing crystals are likely to form a rigid interlocking framework that should separate the basalt from the crustal melt (Sparks & Marshall 1986). For example, such a chill formed during the emplacement of the Skaergaard intrusion (Wager & Brown 1968), and would have allowed very little contamination of the basaltic magma by melting of the Precambrian gneiss country rock (Stewart & DePaolo 1990).

If, however, the melting of warmer crust leads to an unconsolidated pile of basaltic crystals, and if the slope of this crystal pile exceeds its angle of repose, then the crystals may be able to flow down the slope in a manner similar to the cold fluid shown in figure 15. In this situation, the accumulation of most or all of the crystals at the base of the magma chamber may enable significant contamination of the magma through continued melting of the upper parts of the sloping floor. As an example of where this process may have occurred, I note that the Kiglapait magma failed to chill against its country rocks (Morse 1969, p. 39), and has experienced a greater degree of contamination than the Skaergaard (DePaolo 1985). A potential location for the melting that caused this contamination (with Archean gneiss and migmatite) may be the eastern edge of the Kiglapait, where both the Outer Border Zone and the lowermost stratigraphy of the Lower Zone were apparently unable to accumulate on the nearly vertical floor (More 1969, pp. 36–39, 64–66).

### 5.5. *Melting a stoped block*

Another mechanism that may contaminate a basaltic magma arises through the sinking and simultaneous melting of crustal blocks dislodged from the roof of the magma chamber (Campbell & Turner 1987; Huppert & Sparks 1988*c*). This process,

which was given the name *piecemeal stoping* by Daly (1933), requires the fracturing of the roof into angular blocks that are likely to vary considerably in size. As noted earlier, the basalt will be initially intruded at a depth at which its density is comparable to that of the crust ($\rho_f \approx \rho_s$). Since the settling of stoped blocks requires that they are denser than the magma, it is likely that stoping occurs due to either the sinking of the denser and more refractory portions of an inhomogeneous roof, or due to the bulk magma density having been decreased by a combination of crystal fractionation, crustal assimilation or volatile exsolution.

Consider now the sinking of stoped blocks under a small density difference which is taken to be $\Delta\rho = 0.05$ g cm$^{-3}$. For simplicity, the effects of shape on the settling of the blocks (e.g. Kerr & Lister 1991) will not be considered, and they will be assumed to be spherical, with a radius $R$ and a settling velocity $V_b$ that is given by Stokes law

$$V_b = 2g\Delta\rho R^2/(9\mu_f). \tag{37}$$

This law is valid provided that the Reynolds number $2R\rho_f V_b/\mu_f$ is less than about 1, a condition that is satisfied for blocks with diameters that are less than about a metre. Given the estimate of critical upslope distance $H_c \approx 10$ m in §5.4, it can also be expected that blocks that are smaller than this dimension will have laminar flow in their compositional boundary layers. If the falling of the blocks leads to efficient heat transfer but does not influence the motion of the compositional boundary layer, the blocks will melt at a mean velocity, calculated in Appendix C, that is given by

$$-\mathrm{d}R/\mathrm{d}t = A/R^{1/4}, \tag{38}$$

where

$$A = 1.17127K\left(\frac{k_m(T_f - T_m)}{(\rho_s L_s + \rho_s c_s(T_m - T_s))}\right)^{3/4}\left(\frac{g(\rho_f - \rho_m)}{2\mu_m}\right)^{1/4}. \tag{39}$$

Integration of (38) shows that a sphere of initial radius $R_0$ will melt in a time

$$t = 4R_0^{5/4}/(5A), \tag{40}$$

while substitution of $R(t)$ in (37) reveals that, during this time, it will fall a distance

$$z = 8g\,\Delta\rho\, R_0^{13/4}/(117A\mu_f). \tag{41}$$

From (41), and assuming a value of $K = 1/\sqrt{2}$, it is found that stoped blocks with diameters that are smaller than about 0.5 m would melt before they could reach the base of a magma chamber that is 1 km in height.

There is, however, a major flaw in the above calculation: namely, that in (37) the buoyancy of the compositional boundary layer has been ignored. Indeed, in the case of the 0.5 m diameter block discussed above, (C4) indicates that the compositional boundary layer will have a typical thickness of about 11 cm, and a buoyancy that is about 16 times greater than the weight of the block! Consequently, rather than sinking, the block will come to rest at the interface between the basaltic and granitic magmas (see figure 20). At the interface, the block will melt in a few hours, releasing granitic magma that will flow around the block and into the granitic layer without being able to mix with the basaltic magma.

For a stoped block to actually be able to sink in the chamber, it will need to be $\sim 10$ m in diameter. Such a large block will not melt significantly during its traverse of the magma chamber. It subsequent melting behaviour, like that of the rest of the chamber floor, will then be inhibited by crystal deposition (as discussed earlier in §§5.2

and 5.4). It is therefore concluded that stoping will probably be responsible for only minor crustal contamination of a basaltic magma.

## 6. Conclusions

In this paper I have used a scaling analysis to quantify the rate at which a horizontal solid melts in the presence of vigorous compositional convection. For the analysis to be valid, two conditions need to be satisfied. The first condition expresses the fact that the heat flux to the boundary can only be accurately estimated (by (16)) if the thickness of the thermal boundary layer is large in comparison to the thickness of the melt layer. This condition is satisfied if the Stefan number is sufficiently large ($\mathscr{S} \gtrsim k_f/k_m$). If instead the Stefan number is very small, then the temperature profile is very nonlinear (see Appendix A), and the melting rate is approximately proportional to $\ln^{2/3}(1/\mathscr{S})$.

The second condition arises from the assumption that the compositional flux to the boundary can be neglected, and is satisfied if the Stefan number is not too large ($\mathscr{S} \ll (\kappa_f/D)^{1/2}$). For larger $\mathscr{S}$, the significant compositional flux to the boundary reflects a transition, from melting to dissolving, that is described by a scaling analysis given in the Appendix to Kerr (1994).

Several series of laboratory experiments were then performed in which wax and ice blocks were melted by hot aqueous solutions. The observed melting velocities were consistent with the scaling theory, with a constant of proportionality that is increased by the release of heat during mixing of the melted solid with the convecting fluid. Additional experiments showed that the regime of vigorous compositional convection will occur only if the buoyancy ratio defined by (18) is greater than about 2.0 on a horizontal floor, and about 2.7 on a floor inclined at 30°.

In recent years there has been a considerable effort to understand the thermal and compositional evolution of large magmatic bodies in the Earth's crust, and to interpret the final solidified igneous rocks (Turner & Campbell 1986). The current study is motivated by the desire to predict the extent to which hot basaltic magmas can melt and mix with the crust into which they are intruded (Campbell & Turner 1987; Huppert & Sparks 1988*a*). The earlier study of Huppert & Sparks (1988*b*, *c*) has shown that a basaltic magma chamber can melt its roof at a rate of a few metres per year. This melting creates a convecting layer of buoyant crustal melt, which can slowly affect the composition of the underlying basalt by either chemical diffusion through the double-diffusive interface (e.g. Lesher 1990; Stewart & DePaolo 1992) or by crystals in the granitic magma falling through this interface.

In contrast to the melting at the roof, the melting of the floor and walls of a magma chamber, and the melting of roof blocks that fall into the chamber, are all determined by *compositional* rather than thermal convection. At the floor of the chamber, the analysis presented in §5.2 suggests that the vigour of compositional convection, and hence the rate and extent of melting and magma mixing, is likely to be rapidly suppressed by the growth and deposition of dense crystals in the basaltic magma. A similar suppression of melting is also likely to occur on a sloping floor, unless the slope exceeds the angle of repose of the pile of depositing crystals (see §5.4). On a sloping roof (§5.3), the results of an additional scaling analysis and laboratory experiment predict a typical melting velocity of about 23 m per year, a rate which is significantly faster than that at a horizontal roof. This melting is unlikely however to lead to significant direct mixing of the two magmas since the flow in the compositional boundary layer is laminar. Finally, an examination of the melting of stoped blocks (§5.5) suggests that metre-size blocks will be prevented from sinking by the buoyancy

of their compositional boundary layers, and that the sinking of much larger blocks is likely to cause only limited contamination of the basaltic magma.

I thank Ian Campbell, Herbert Huppert, John Lister, Stewart Turner, Andy Woods and Grae Worster for many helpful comments, and Tony Beasley, Derek Corrigan and Ross Wylde-Browne for their technical assistance with the experiments. The work was aided by a visit to the Institute of Theoretical Geophysics, Cambridge, that was made possible by the generous financial support of The British Council.

## Appendix A. Melting at small Stefan numbers

When $\mathscr{S} \ll k_f/k_m$, rapid movement of the interface produces a melt layer whose thickness $h_m$ is much greater than the distance $h_T$ over which heat can diffuse. As a consequence, the temperature profile through the melt layer will be very nonlinear, and is approximately given by

$$T(z) \approx T_m + (T_f - T_m)\, \mathrm{e}^{-V(h_m+z)/\kappa_m}, \quad \text{where} \quad 0 > z > -h_m. \tag{A 1}$$

The heat flux $F$ to the interface is

$$F \approx \rho_m c_m V(T_f - T_m)\, \mathrm{e}^{-Vh_m/\kappa_m}, \tag{A 2}$$

which when combined with (9) gives

$$\mathscr{S}_m \approx \mathrm{e}^{-Vh_m/\kappa_m}, \tag{A 3}$$

where the Stefan number $\mathscr{S}_m$ is defined by

$$\mathscr{S}_m = \frac{\rho_s L_s + \rho_s c_s (T_m - T_s)}{\rho_m c_m (T_f - T_m)}. \tag{A 4}$$

When (4) is then substituted into (A 3), the asymptotic law

$$V \sim \left(\frac{g(\rho_f - \rho_m)\kappa_m^2}{P\mu_m}\right)^{1/3} \ln^{2/3}\left(\frac{1}{\mathscr{S}_m}\right) \tag{A 5}$$

is obtained for $\mathscr{S}_m \ll 1$.

The singularity in (A 5) can be compared with the behaviour during diffusively controlled melting of a solid at small Stefan number. In this case, the interfacial position $X$ as a function of time $t$ is given by

$$X = 2\lambda(\kappa t)^{1/2}, \tag{A 6}$$

where $\lambda$ is the root of

$$\frac{\mathrm{e}^{-\lambda^2}}{1 + \operatorname{erf}\lambda} - \frac{(T_m - T_s)\, \mathrm{e}^{-\lambda^2}}{(T_f - T_m)\operatorname{erfc}\lambda} = \frac{\lambda L \pi^{1/2}}{c(T_f - T_m)} \tag{A 7}$$

(Carslaw & Jaeger 1986, §11, equation (33)). When $\lambda$ is large,

$$\operatorname{erfc}\lambda \approx \mathrm{e}^{-\lambda^2}/(\lambda\pi^{1/2}) \tag{A 8}$$

and $\operatorname{erf}\lambda \approx 1$. Equation (A 7) therefore becomes

$$\tfrac{1}{2}\mathrm{e}^{-\lambda^2} \approx \lambda\pi^{1/2}\mathscr{S}, \tag{A 9}$$

where

$$\mathscr{S} = \frac{L + c(T_m - T_s)}{c(T_f - T_m)}, \tag{A 10}$$

which allows $\lambda$ to be estimated as

$$\lambda \approx \ln^{1/2}\left(\frac{1}{2\pi^{1/2}\mathscr{S}}\right). \tag{A 11}$$

## Appendix B. Melting an ice roof

Consider the simple case of the melting of an ice roof by a dilute aqueous solution of ethanol. In this case I use a Boussinesq approximation that the physical properties of the melt and fluid are equal except for their densities. It is also assumed that $\mathscr{S} \gg 1$, for which the theory in §2 predicts the velocity $V_c$ for compositionally driven melting as

$$V_c \propto \left(\frac{g\Delta\rho_c \kappa^2}{10.2998\mu\mathscr{S}^4}\right)^{1/3}, \tag{B 1}$$

where the compositional density difference $\Delta\rho_c = \rho_f - \rho_m$. The IR experiments suggest that the constant of proportionality in this expression is about 0.50 (see figure 8).

Alternatively, if the melting is dominated by vigorous thermal convection rather than vigorous compositional convection, then the heat flux $F_T$ to the interface is given by (32), and the corresponding melting velocity $V_T$ is

$$V_T = \frac{0.156}{\mathscr{S}}\left(\frac{g\Delta\rho_T \kappa^2}{\mu}\right)^{1/3}, \tag{B 2}$$

where the thermal density difference $\Delta\rho_T = \rho\alpha(T_f - T_m)$.

It is noted that both (B 1) and (B 2) are proportional to $(T_f - T_m)^{4/3}$, and that the ratio of these velocities is given by

$$\frac{V_c}{V_T} = 1.47\left(\frac{\Delta\rho_c}{\Delta\rho_T \mathscr{S}}\right)^{1/3}. \tag{B 3}$$

Since $\mathscr{S}$ measures the relative thicknesses of the thermal and compositional boundary layers (see §2), we obtain the simple and physically intuitive result that the melting is dominated by compositional convection ($V_c \gg V_T$) if the compositional buoyancy $\Delta\rho_c h_m$ is much greater than the thermal buoyancy $\Delta\rho_T h_T$ (i.e. if $\mathscr{R} \gg 1$).

For experiment IR1, $\Delta\rho_c$ and $\Delta\rho_T \mathscr{S}$ are both equal to about 0.005 g cm$^{-3}$. The melting is therefore driven equally by thermal and compositional convection, and occurs at a rate somewhat faster than is predicted solely by either $V_c$ or $V_T$ (see table 2).

## Appendix C. Melting of a sphere or cylinder

In this appendix, I extend the scaling analysis given in §5.3 to describe the melting, driven by compositional convection, of either a stationary sphere or horizontal cylinder. In both cases, the thickness $h$ of the compositional boundary layer remains linked to the melting velocity $V$ and the characteristic alongslope velocity $U$ by

$$(\rho_s L_s + \rho_s c_s(T_m - T_s))\, V = k_m(T_f - T_m)/h \tag{C 1}$$

and

$$\mu_m U/h^2 \sim g \sin\beta(\rho_f - \rho_m), \tag{C 2}$$

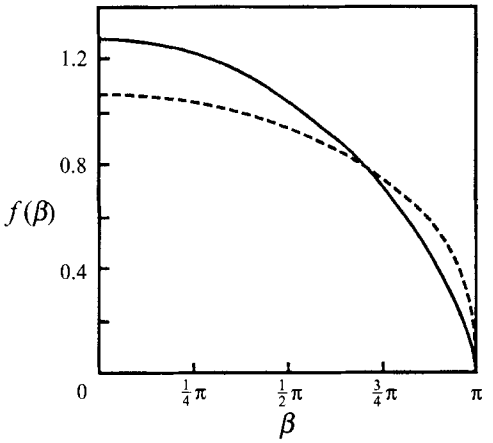


FIGURE 21. The function $f(\beta)$, defined by (C6), for a sphere (solid curve) and for a cylinder (dashed curve). At $\beta = 0$, $f(\beta)$ has respective values of $(\frac{8}{3})^{1/4}$ and $(\frac{4}{3})^{1/4}$.

where $\beta$ is the angle to the vertical. At a distance $z = R\beta$ upslope from the base, conservation of mass requires that

$$\mathrm{d}Q/\mathrm{d}z = 2\pi R \sin\beta V, \quad \text{where} \quad Q \sim 2\pi R \sin\beta U h, \tag{C 3a}$$

for a sphere, and

$$\mathrm{d}Q/\mathrm{d}z = V, \quad \text{where} \quad Q \sim Uh, \tag{C 3b}$$

for a cylinder. Combining (C1)–(C3), followed by integration using both substitution and a separation of variables, then yields

$$h = \frac{1}{Kf(\beta)}\left(\frac{\mu_m k_m (T_f - T_m) R}{g(\rho_f - \rho_m)(\rho_s L_s + \rho_s c_s (T_m - T_s))}\right)^{1/4} \tag{C 4}$$

and

$$V = Kf(\beta)\left(\frac{k_m (T_f - T_m)}{(\rho_s L_s + \rho_s c_s (T_m - T_s))}\right)^{3/4}\left(\frac{g(\rho_f - \rho_m)}{\mu_m R}\right)^{1/4}, \tag{C 5}$$

where $K$ is a constant and the function $f(\beta)$ is given by

$$f(\beta) = \left(\sin^{8/3}\beta \Big/ \left(\int_0^\beta \sin^{5/3}\beta' \,\mathrm{d}\beta'\right)\right)^{1/4} \tag{C 6a}$$

for a sphere, and

$$f(\beta) = \left(\sin^{4/3}\beta \Big/ \left(\int_0^\beta \sin^{1/3}\beta' \,\mathrm{d}\beta'\right)\right)^{1/4} \tag{C 6b}$$

for a cylinder. Evaluation of $f(\beta)$, which is graphed in figure 21, shows that it decreases slowly in the range $0 < \beta < \frac{1}{2}\pi$, because the increase in $Q$ with distance upslope is mostly accommodated by the increase in $U$ with increasing slope (and also by the increase in the cross-sectional area $2\pi R \sin\beta h$ in the case of a sphere). The function then increases rapidly as $\beta$ approaches $\pi$. These results are consistent with observations of the variation in thickness of the laminar boundary layer due thermal convection from a horizontal cylinder (e.g. figure 14.1 of Tritton 1977).

It is also noted that (C4) and (C5) are very similar to (30) and (31), with the only difference being that $\sin^{1/4}\beta$ is replaced by $f(\beta)$. The expressions correspond to an average heat flux, non-dimensionalized by $k_m(T_f - T_m)/(2R)$, that is given by $Nu_m =$

$1.171\,27K(\mathscr{S}_m\,Ra_m)^{1/4}$ for a sphere, and by $Nu_m = 1.029\,57K(\mathscr{S}_m\,Ra_m)^{1/4}$ for a cylinder, where the Rayleigh number is given by $Ra_m = g(\rho_f - \rho_m)(2R)^3/(\kappa_m\mu_m)$. These results are analogous to $Nu \sim Ra^{1/4}$ expressions for laminar convection on a sphere (Clift, Grace & Weber 1978, p. 252; Jafarpur & Yovanovich 1992) and on a cylinder (Bird, Stewart & Lightfoot 1960, p. 413).

## REFERENCES


Bird, R. B., Stewart, W. E. & Lightfoot, E. N. 1960 *Transport Phenomena.* John Wiley & Sons.

Brandeis, G. & Jaupart, C. 1986 On the interaction between convection and crystallization in cooling magma chambers. *Earth Planet. Sci. Lett.* **77**, 345–361.

Brandeis, G., Jaupart, C. & Allègre, C. J. 1984 Nucleation, crystal growth and the thermal regime of cooling magmas. *J. Geophys. Res.* **89**, 10161–10177.

Bruce, P. M. & Huppert, H. E. 1989 Thermal control of basaltic fissure eruptions. *Nature* **342**, 665–667.

Campbell, I. H. 1977 A study of macro-rhythmic layering and cumulate processes in the Jimberlana intrusion, Western Australia. I. The upper layered series. *J. Petrol.* **18**, 183–215.

Campbell, I. H. 1985 The difference between oceanic and continental tholeiites: a fluid dynamic explanation. *Contrib. Mineral. Petrol.* **91**, 37–43.

Campbell, I. H. 1986 A fluid dynamic model for potholes of the Merensky Reef. *Econ. Geol.* **81**, 1118–1125.

Campbell, I. H. & Turner, J. S. 1987 A laboratory investigation of assimilation at the top of a basaltic magma chamber. *J. Geol.* **95**, 155–172.

Carslaw, H. S. & Jaeger, J. C. 1986 *Conduction of Heat in Solids.* Oxford University Press.

Carte, A. E. 1961 Air bubbles in ice. *Proc. Phys. Soc.* **77**, 757–768.

Clift, R., Grace, J. R. & Weber, M. E. 1978 *Bubbles, Drops and Particles.* Academic Press.

Cox, K. G. & Mitchell, C. 1988 Importance of crystal settling in the differentiation of Deccan Traps basaltic magmas. *Nature* **333**, 447–449.

Daly, R. A. 1933 *Igneous Rocks and the Depths of the Earth.* Hafner.

Davaille, A. & Jaupart, C. 1993 Transient high Rayleigh number thermal convection with large viscosity variations. *J. Fluid Mech.* **253**, 141–166.

DePaolo, D. J. 1985 Isotopic studies of processes in mafic magma chambers: I. The Kiglapait Intrusion, Labrador. *J. Petrol.* **26**, 925–951.

Fang, D. & Hellawell, A. 1988 The surface morphology of crystals melting under solutions of different densities. *J. Cryst. Growth* **92**, 364–370.

Fink, J. H. & Griffiths, R. W. 1990 Radial spreading of viscous-gravity currents with solidifying crust. *J. Fluid Mech.* **221**, 485–509.

Huppert, H. E. 1989 Phase changes following the initiation of a hot turbulent flow over a cold solid surface. *J. Fluid Mech.* **198**, 293–320.

Huppert, H. E. & Sparks, R. S. J. 1985 Cooling and contamination of mafic and ultramafic magmas during ascent through continental crust. *Earth Planet. Sci. Lett.* **74**, 371–386.

Huppert, H. E. & Sparks, R. S. J. 1988*a* The fluid dynamics of crustal melting by injection of basaltic sills. *Phil. Trans. R. Soc.: Edinb. Earth Sci.* **79**, 237–243.

Huppert, H. E. & Sparks, R. S. J. 1988*b* Melting the roof of a chamber containing a hot, turbulently convecting fluid. *J. Fluid Mech.* **188**, 107–131.

Huppert, H. E. & Sparks, R. S. J. 1988*c* The generation of granitic magmas by intrusion of basalt into continental crust. *J. Petrol.* **29**, 599–624.

Irvine, T. N. 1970 Heat transfer during solidification of layered intrusions. I. Sheets and sills. *Can. J. Earth. Sci.* **7**, 1031–1061.

Jafarpur, K. & Yovanovich, M. M. 1992 Laminar free convective heat transfer from isothermal spheres: a new analytical method. *Intl J. Heat Mass Transfer* **35**, 2195–2201.

Katsaros, K. B., Liu, W. T., Businger, J. A. & Tillman, J. E. 1977 Heat transport and thermal structure in the interfacial boundary layer measured in an open tank of water in turbulent free convection. *J. Fluid Mech.* **83**, 311–335.

KERR, R. C. 1994 Dissolving driven by vigorous compositional convection. *J. Fluid Mech.* **280**, 287–302.

KERR, R. C. & LISTER, J. R. 1991 The effects of shape on crystal settling and on the rheology of magmas. *J. Geol.* **99**, 457–467.

KERR, R. C. & LISTER, J. R. 1992 Further results for convection driven by the differential sedimentation of particles. *J. Fluid Mech.* **243**, 227–245.

KUO, L.-C. & KIRKPATRICK, R. J. 1985 Kinetics of crystal dissolution in the system diopside-forsterite-silica. *Am. J. Sci.* **285**, 51–90.

LESHER, C. E. 1990 Decoupling of chemical and isotopic exchange during magma mixing. *Nature* **344**, 235–237.

LISTER, J. R. 1990 Buoyancy-driven fluid fracture: similarity solutions for the horizontal and vertical propagation of fluid-filled cracks. *J. Fluid Mech.* **217**, 213–239.

LISTER, J. R. & KERR, R. C. 1989 The effect of geometry on the gravitational instability of a buoyant region of viscous fluid. *J. Fluid Mech.* **202**, 577–594.

LISTER, J. R. & KERR, R. C. 1991 Fluid-mechanical models of crack propagation and the application to magma transport in dykes. *J. Geophys. Res.* **96**, 10049–10077.

MARTIN, D. & CAMPBELL, I. H. 1988 Laboratory modeling of convection in magma chambers: crystallization against sloping floors. *J. Geophys. Res.* **93**, 7974–7988.

MARTIN, D. & NOKES, R. 1988 Crystal settling in a vigorously convecting magma chamber. *Nature* **332**, 534–536.

MARTIN, D. & NOKES, R. 1989 A fluid-dynamical study of crystal settling in convecting magmas. *J. Petrol.* **30**, 1471–1500.

MORSE, S. A. 1969 Geology of the Kiglapait Intrusion, Labrador. *Mem. Geol. Soc. Am.* **112**.

NILSON, R. H., MCBIRNEY, A. R. & BAKER, B. H. 1985 Liquid fractionation. Part II: Fluid dynamics and quantitative implications for magmatic systems. *J. Volcanol. Geotherm. Res.* **24**, 25–54.

ODÉ, H. 1966 Gravitational instability of a multi-layered system. PhD thesis, University of Utrecht.

OXTOBY, D. W. 1990 New perspectives on freezing and melting. *Nature* **347**, 725–730.

PHILPOTTS, A. R. & ASHER, P. M. 1993 Wallrock melting and reaction effects along the Higganum Diabase Dyke in Connecticut: contamination of a continental flood basalt feeder. *J. Petrol.* **34**, 1029–1058.

RYAN, M. P. 1987 Neutral buoyancy and the mechanical evolution of magmatic systems. In *Magmatic Processes: Physicochemical Principles,* Spec. Publ. 1 (ed. B. O. Mysen), pp. 259–287. The Geochemical Society, University Park, PA.

SPARKS, R. S. J. & HUPPERT, H. E. 1984 Density changes during fractional crystallization of basaltic magmas: fluid dynamic implications. *Contrib. Mineral. Petrol.* **85**, 300–309.

SPARKS, R. S. J. & MARSHALL, L. A. 1986 Thermal and mechanical constraints on mixing between mafic and silicic magmas. *J. Volcanol. Geotherm. Res.* **29**, 99–124.

STEWART, B. W. & DEPAOLO, D. J. 1990 Isotopic studies of processes in mafic magma chambers: II. The Skaergaard Intrusion, East Greenland. *Contrib. Mineral. Petrol.* **104**, 125–141.

STEWART, B. W. & DEPAOLO, D. J. 1992 Diffusive isotopic contamination of mafic magma by coexisting silicic liquid in the Muskox Intrusion. *Science* **255**, 708–711.

TRITTON, D. J. 1977 *Physical Fluid Dynamics.* Van Nostrand Reinhold.

TURNER, J. S. 1979 *Buoyancy Effects in Fluids.* Cambridge University Press.

TURNER, J. S. & CAMPBELL, I. H. 1986 Convection and mixing in magma chambers. *Earth Sci. Rev.* **23**, 255–352.

WAGER, L. R. & BROWN, G. M. 1968 *Layered Igneous Rocks.* Edinburgh: Oliver & Boyd.

WASHBURN, E. W. (ed.) 1926 *International Critical Tables of Numerical data: Physics, Chemistry and Technology.* National Academic Press.

WEAST, R. C. (ed.) 1989 *CRC Handbook of Chemistry and Physics.* CRC Press.

WILSON, J. R. & LARSEN, S. B. 1985 Two-dimensional study of a layered intrusion: the Hyllingen Series, Norway. *Geol. Mag.* **122**, 97–124.

WOODS, A. W. 1991 Fluid mixing during melting. *Phys. Fluids* A **3**, 1393–1404.

WOODS, A. W. 1992 Melting and dissolving. *J. Fluid Mech.* **239**, 429–448.